CHAPTER 121

Nanoelectromechanical Systems and Modeling

Changhong Ke, Horacio D. Espinosa
Department of Mechanical Engineering, Northwestern University, Illinois, USA

CONTENTS

1. Introduction 1
2. Nanoelectromechanical Systems 2
    2.1. Carbon Nanotubes 2
    2.2. Fabrication Methods 3
    2.3. Inducing and Detecting Motion 6
    2.4. Functional Nanoelectromechanical Systems Devices 6
    2.5. Future Challenges 18
3. Modeling of Nanoelectromechanical Systems Devices 20
    3.1. Multiscale Modeling 21
    3.2. Continuum Mechanics Modeling 24
    References 36

1. INTRODUCTION

Nanoelectromechanical systems (NEMS) are made of electromechanical devices that have critical dimensions from hundreds to a few nanometers. By exploring nanoscale effects, NEMS present interesting and unique characteristics, which deviate greatly from their predecessor microelectromechanical systems (MEMS). For instance, NEMS-based devices can have fundamental frequencies in microwave range (~100 GHz) [1]; mechanical quality factors in the tens of thousands, meaning low-energy dissipation; active mass in the femtogram range; force sensitivity at the attonewton level; mass sensitivity up to attogram [2] and sub-attogram [3] levels; heat capacities far below a "yoctocalorie" [4]; power consumption in the order of 10 attowatts [5]; extreme high integration level, approaching 10^{12} elements per square centimeter [1]. All these distinguished properties of NEMS devices pave the way to applications such as force sensors, chemical sensors, biological sensors, and ultrahigh-frequency resonators.

The interesting properties of the NEMS devices typically arise from the behavior of the active parts, which, in most cases, are in the forms of cantilevers or doubly clamped beams with dimensions at nanometer scale. The materials for those active components include

ISBN: 1-58883-042-X/$35.00
Copyright © 2005 by American Scientific Publishers
All rights of reproduction in any form reserved.
Handbook of Theoretical and Computational Nanotechnology
Edited by Michael Rieth and Wolfram Schommers
Volume 1: Pages (1–38)

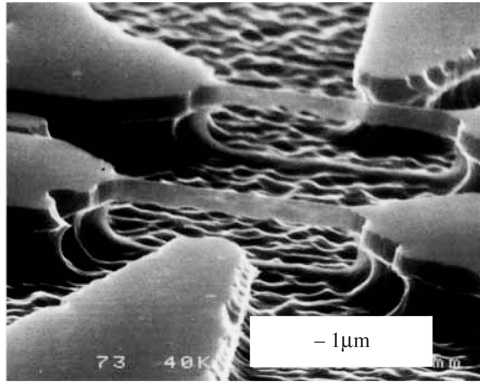

Figure 1. SEM Image of an undercut Si beam, with length of 7.7 μm, width of 0.33 μm and height of 0.8 μm. Reprinted with permission from [6], A. N. Cleland and M. L. Roukes, *Appl. Phys. Lett.* 69, 2653 (1996). © 1996, American Institute of Physics.

silicon and silicon carbide, carbon nanotubes, and gold and platinum, to name a few. Silicon is the basic material for integrated circuit (IC) technology during the past few decades, and MEMS and is widely used to build NEMS. Figure 1 is a scanning electron microscopy (SEM) image of a double-clamped resonator fabricated from a bulk, single-crystal silicon substrate [6]. However, ultrasmall silicon-based NEMS fail to achieve desired high-quality factors because of the dominance of surface effects, such as surface oxidation and reconstruction, and thermoelastic damping. Limitations in strength and flexibility also compromise the performance of silicon-based NEMS actuators. Instead, carbon nanotubes can well represent the ideas of NEMS, given their nearly one-dimensional structures with high-aspect ratio, perfect terminated surfaces, and excellent electrical and mechanical properties. Because of significant advances in growth, manipulation, and knowledge of electrical and mechanical properties, carbon nanotubes have become the most promising building blocks for the next generation of NEMS. Several carbon nanotube–based functional NEMS devices have been reported so far [1, 7–12]. Similar to carbon nanotubes, nanowires are another type of one-dimensional novel nanostructure for building NEMS because of their size and controllable electrical properties.

This chapter provides a comprehensive review of NEMS devices to date and summarizes the modeling currently being pursued to gain insight into their performance. This chapter is organized as follows: in the first part, we review the carbon nanotubes and carbon nanotube–based NEMS. We also discuss nanowires-based NEMS. In the second part, we present the modeling of NEMS, including multiscale modeling and continuum modeling.

2. NANOELECTROMECHANICAL SYSTEMS

2.1. Carbon Nanotubes

Carbon nanotubes exist as a macromolecule of carbon, analogous to a sheet of graphite rolled into a cylinder. They were discovered by Sumio Iijima in 1991 and are a subset of the family of fullerene structures [13]. The properties of the nanotubes depend on the atomic arrangement (how sheets of graphite are rolled to form a cylinder), their diameter, and their length. They are light, stiff, flexible, thermally stable, and chemically inert. They have the ability to be either metallic or semiconducting depending on the "twist" of the tube, which is called "chirality" or "helicity." Nanotubes may exist as either single-walled or multiwalled structures. Multiwalled carbon nanotubes (MWNTs) (Fig. 2(B)) are simply composed of multiple concentric single-walled carbon nanotubes (SWNTs) (Fig. 2(A)) [14]. The spacing between the neighboring graphite layers in MWNTs is $\sim$0.34 nm. These layers interact with each other via van der Waals forces.

The methods to synthesize carbon nanotubes include electric arc-discharge [15, 16], laser ablation [17], and catalytic chemical vapor deposition (CVD) methods [18]. During synthesis, nanotubes are usually mixed with residues, including various types of carbon particles.

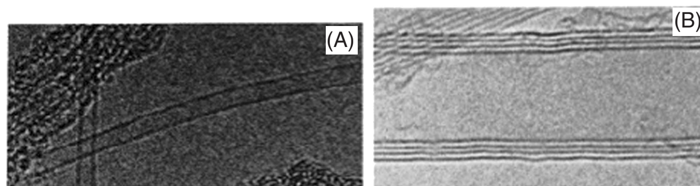

Figure 2. High-resolution transmission electron microscopy image of typical single-walled carbon nanotubes (SWNT) (A) and multi-walled carbon nanotubes (MWNT) (B). Reprinted with permission from [14], P. Ajayan, *Chem. Rev.* 99, 1787 (1999). © 1999, American Chemical Society.

For most applications and tests, a purification process is required. In one of the most common approaches, nanotubes are ultrasonically dispersed in a liquid (e.g., isopropanol) and the suspension is centrifuged to remove large particles. Other methods, including dielectrophoretic separation, are being developed to provide improved yield.

The mechanical and electrical properties of carbon nanotubes have been under intensive study during the past decade. Qian et al. [19] contributed a comprehensive review article, "Mechanics of Carbon Nanotube," from the perspective of both experimentation and modeling. The electronics of carbon nanotubes is extensively reviewed by McEuen et al. [20]. Besides, the study of the coupled electromechanical properties, which are essential to NEMS, is rapidly progressing. Some interesting results have been reported regarding the fact that the electrical properties of carbon nanotubes are sensitive to the structure variation and can be changed dramatically because of the change of the atomic bonds induced by mechanical deformations. It is known that carbon nanotubes can even change from metallic to semiconducting when subjected to mechanical deformation [21–23].

2.2. Fabrication Methods

The fabrication processes of NEMS devices can be categorized according to two approaches. *Top-down* approaches, that evolved from manufacturing of MEMS structures, use submicron lithographic techniques, such as electron-beam lithography, to fabricate structures from bulk materials, either thin films or bulk substrates. *Bottom-up* approaches fabricate the nanoscale devices by sequentially assembling of atoms and molecules as building blocks. Top-down fabrication is size limited by facts such as the resolution of the electron-beam lithography, etching-induced roughness, and synthesis constraints in epitaxially grown substrates. Significant interest has been shown in the integration of nanoscale materials such as carbon nanotubes and nanowires, fabricated by bottom-up approaches, to build nanodevices. Most of the nanodevices reported so far in the literature are obtained by "hybrid" approaches, that is, combination of bottom-up (self assembly) and top-down (lithographic) approaches [24].

One of the key and most challenging issues of building carbon nanotubes–based or nanowires-based NEMS is the positioning of nanotubes or nanowires at the desired locations with high accuracy and high throughput. Reported methods of manipulation and positioning of nanotubes are briefly summarized in the following section.

2.2.1. Random Dispersion Followed by E-Beam Lithography

After purification, a small aliquot of a nanotube suspension is deposited onto a substrate. The result is nanotubes randomly dispersed on the substrate. Nanotubes on the substrate are imaged inside a scanning electron microscope (SEM) and then this image is digitized and imported to a mask-drawing software, where the mask for the subsequent electron-beam lithography is designed. In the mask layout, pads are designed to superimpose over the carbon nanotubes. Wet etching is employed to remove the material under the carbon nanotubes to form freestanding nanotube structures. This process requires an alignment capability in the lithographic step with an accuracy of 0.1 μm or better. This method was firstly employed to make nanotube structures for mechanical testing [25, 26]. The reported NEMS devices based on this method include nanotube–based rotational actuators [9] and nanowire-based resonators [24].

2.2.2. Nanomanipulation

Manipulation of individual carbon nanotubes using piezo-driven manipulators inside electron microscope chambers is one of the most commonly used methods to build NEMS [8] and structures for mechanical testing [27–32]. In general, the manipulation and positioning of nanotubes is accomplished in the following manner: (1) a source of nanotubes is positioned close to the manipulator inside the microscope; (2) the manipulator probe is moved close to the nanotubes under visual surveillance of the microscope monitor until a protruding nanotube is attracted to the manipulator due to either van der Waals forces or electrostatic forces; (3) the free end of the attracted nanotube is "spot welded" by the electron-beam-induced deposition (EBID) of hydrocarbon [8, 31] or metals, like platinum [32] from adequate precursor gases.

Figure 3 shows a three-dimensional nanomanipulator (Klocke Nanotechnik Co.) having the capability of moving in X, Y, and Z directions with nanometer displacement resolution. The manipulation process of an individual carbon nanotube is illustrated in Fig. 4(A)–4(C).

2.2.3. External Field Alignment

DC/AC electric fields have been successfully used in the manipulation of nanowires [33], nanotubes [34, 35], and bioparticles [36–39]. Microfabricated electrodes are typically used to create an electric field in the gap between them. A droplet containing carbon nanotubes in suspension is dispensed into the gap with a micropipette. The applied electric field aligns the nanotubes, due to the dielectrophoretic effect, which results in the bridging of the electrodes by a single nanotube. The voltage drop that arises when the circuit is closed (DC component) ensures the manipulation of only one nanotube. Besides, AC dielectrophoresis has been employed to successfully separate metallic from semiconducting single-walled carbon nanotubes in suspension [40]. NEMS devices fabricated using this method include nanotube–based nanorelays [41].

Huang et al. [42] demonstrated another method for aligning nanowires. A laminar flow was employed to achieve preferential orientation of nanowires on chemically patterned surfaces. This method was successfully used in the alignment of silicon nanowires. Magnetic fields have also been used to align carbon nanotubes [43].

2.2.4. Direct Growth

Instead of manipulating and aligning carbon nanotubes after their manufacturing, researchers have also examined methods for controlled direct growth. Huang et al. [44] used the microcontact printing technique to directly grow aligned nanotubes vertically. Dai et al.

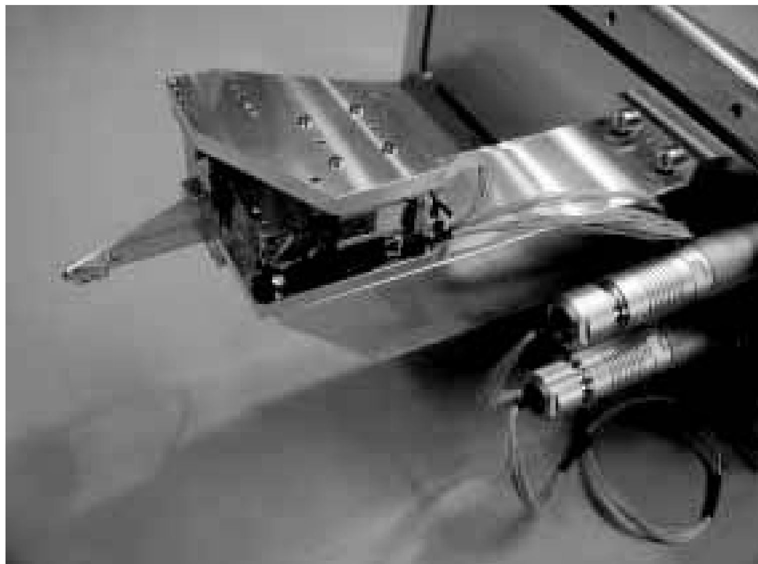

Figure 3. Klocke Nanotechnik nanomanipulator possessing nanometer resolution in the x, y, and z axes.

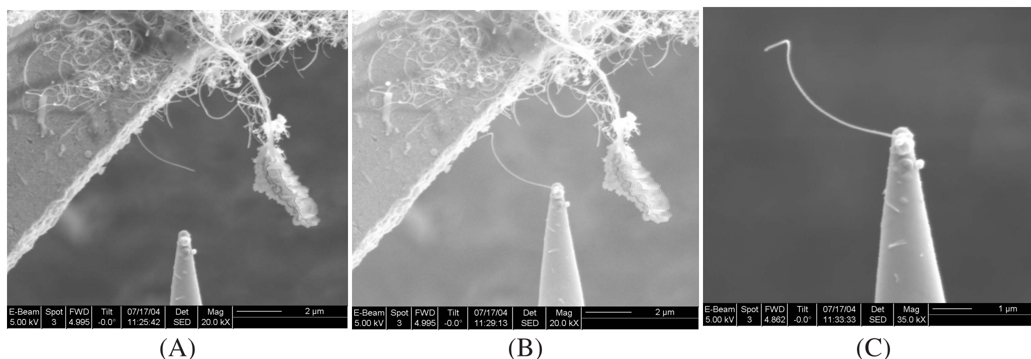

(A) (B) (C)

Figure 4. SEM images of the manipulation of carbon nanotubes using the three-dimensional Klocke Nanotechnik nanomanipulator. (A) Manipulator probe is approaching a protruding nanotube. The sample is dried nanotube solution on top of a TEM copper grid. (B) Manipulator probe makes contact with the free end of the nanotube and the nanotube is welded to the probe by EBID of platinum. (C) A single nanotube mounted to the manipulator probe.

[45–48] reported several patterned growth approaches developed in his group. The idea is to pattern the catalyst in an arrayed fashion and control the growth of carbon nanotubes from specific catalytic sites. The authors successfully carried out patterned growth of both MWNTs and SWNTs and exploited methods including self-assembly and external electric-field control. Figure 5 shows a SEM image of suspended single-walled nanotubes grown by electric-field-directed CVD method [47]. The carbon nanotube–based tunable oscillators, reported in Ref. [12], were fabricated using this method.

2.2.5. Self-Assembly

Self-assembly is a method of constructing nanostructures by forming stable bonds between the organic or nonorganic molecules and substrates. Recently, Rao et al. [49] reported an approach in large-scale assembly of carbon nanotubes with high throughput. Dip Pen Nanolithography (DPN), a technique invented by Mirkin's group [50], was employed to functionalize the specific surface regions either with polar chemical groups such as amino ($-NH_2$/$-NH_3^+$) or carboxyl ($-COOH$/$-COO^-$), or with nonpolar groups such as methyl ($-CH_3$). When the substrate with functionalized surfaces was introduced into a liquid suspension of carbon nanotubes, the nanotubes were attracted toward the polar regions and self-assembled

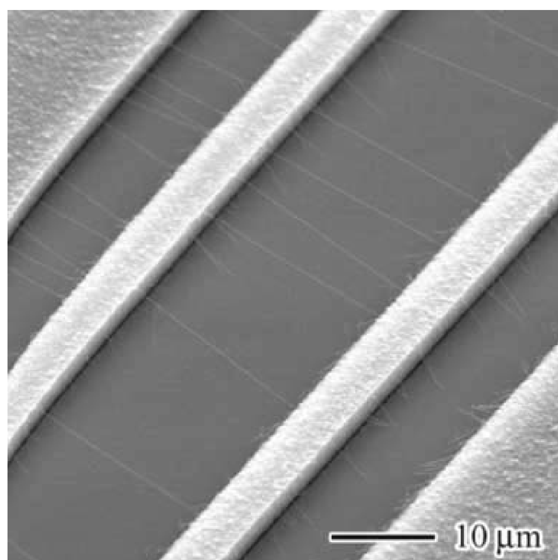

Figure 5. Electric-field-directed freestanding single-walled nanotubes. Reprinted with permission from [47], Y. Zhang et al., *Appl. Phys. Lett.* 79, 3155 (2001). © 2001, American Institute of Physics.

to form predesigned structures, usually within 10 s, with a yield higher than 90%. The reported method is scalable to large arrays of nanotube devices by using high-throughput patterning methods such as photolithography, stamping, or massively parallel DPN.

2.3. Inducing and Detecting Motion

For nanostructures, both inducing and detecting motion are challenging. Some of the methods routinely used in MEMS face challenges when the size shrinks from microscale to nanoscale. For example, optical methods, such as simple-beam deflection schemes or more sophisticated optical and fiber-optical interferometry—both commonly used in scanning probe microscopy to detect the deflection of the cantilevers—generally fall beyond the diffraction limit, which means these methods cannot be applied to objects with cross-section much smaller than the wavelength of light [51].

2.3.1. Inducting Motion

Similar to MEMS, electrostatic actuation of nanostructures by an applied electrical field is commonly used for the actuation of NEMS (e.g., nanotweezers [7, 8]). The Lorenz force has been used to move small conducting beams [6, 24, 52], with alternating currents passing through them in a strong transverse magnetic field. The induced electromotive force, or voltage, can be detected as a measure of the motion. This method requires a fully conducting path and works well with a beam clamped at both ends [53]. Other actuation methods include piezoelectric actuation, thermal actuation using bilayers of materials with different thermal expansion, thermal in-plane actuation due to a specially designed topography [54], and scanning tunneling microscope (STM) [55].

2.3.2. Detecting Motion

The most straightforward method is by direct observation of the motion under electron microscopes [7, 8, 56, 57]. This visualization method, typically with resolution in the nanometer scale, projects the motion in the direction to be perpendicular to the electron beam. Limitations in depth of focus requires that the nano-object motion be primarily in a plane, which normally is coaxial with the electron beam. Electron tunneling is a very sensitive method that can detect subnanometer motion by the exponential dependence of the electron tunneling current on the separation between tunneling electrodes. Therefore, this technique is widely used in NEMS motion detection [5, 12]. Magnetomotive detection is a method based on the presence of an electrostatic field, either uniform or spatially inhomogeneous, through which a conductor is moved. The time-varying flux generates an induced electromotive force in the loop, which is proportional to the motion [24, 52, 58–60]. The displacement detection sensitivity of this technique is less than 1 Å [61]. It is known that carbon nanotubes can act as transistors; as such they can be used to sense their own motion [12, 62]. Capacitance sensors have been widely used in MEMS. They can also be used in NEMS motion sensing with a resolution of a few nanometers [54], and the resolution can be potentially increased to Angstrom range provided that the capacitance measurement can be improved by one order of magnitude.

2.4. Functional Nanoelectromechanical Systems Devices

In this section, we review the carbon nanotubes- or nanowires-based NEMS devices reported in the literature with a special emphasis on fabrication methods, working principles, and applications.

2.4.1. Carbon Nanotube-Based Nanoelectromechanical Systems Devices

2.4.1.1. Nonvolatile Random Access Memory A carbon nanotube–based nonvolatile random access memory (NRAM) reported by Reukes et al. [1] is illustrated in Fig. 6(A). The device is a suspended SWNT crossbar array for both I/O and switchable, bistable device elements with well-defined OFF and ON states. This crossbar consists of a set of parallel SWNTs or nanowires (lower) on a substrate composed of a conducting layer (e.g., highly

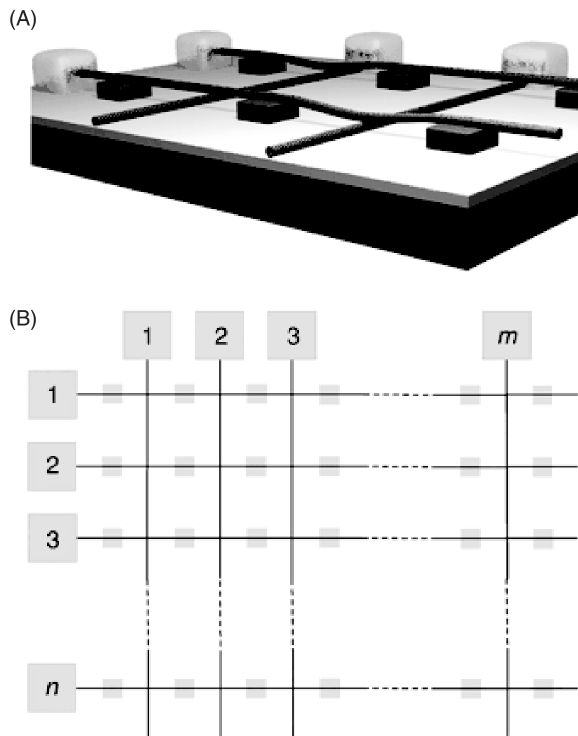

Figure 6. Schematics of freestanding nanotube device architecture with multiplex addressing (A). Three-dimensional view of a suspended crossbar array showing four junctions with two elements in the ON (contact) state and two elements in the OFF (separated) state. (B) Top view of an $n \times m$ device array. Reprinted with permission from [1], T. Rueckes et al., *Science* 289, 94 (2000). © 2000, American Association for the Advancement of Science.

doped silicon [dark gray]) that terminates in a thin dielectric layer (e.g., SiO_2 [light gray]) and a set of perpendicular SWNTs (upper) that are suspended on a periodic array of inorganic or organic supports. Each nanotube is contacted by a metal electrode. Each cross-point in this structure corresponds to a device element with a SWNT suspended above a perpendicular nanoscale wire. Qualitatively, bistability can be envisioned as arising from the interplay of the elastic energy and the van der Waals energy when the upper nanotube is freestanding or the suspended SWNT is deflected and in contact with the lower nanotube. Because the nanotube junction resistance depends exponentially on the separation gap, the separated upper-to-lower nanotube junction resistance will be orders of magnitude higher than that of the contact junction. Therefore, two states—OFF and ON—are well defined. For a device element, these two states can be read easily by measuring the resistance of the junction and, moreover, can be switched between OFF and ON states by applying voltage pulses to nanotubes at corresponding electrodes to produce attractive or repulsive electrostatic forces. A key aspect of this device is that the separation between top and bottom conductors must in the order of 10 nm. In such case, the van der Waals energy overcomes the elastic energy when the junction is actuated (ON state) and remains on this state even if the electrical field is turned off (nonvolatile feature).

The concept of the bitable device was demonstrated by current-voltage (I–V) behaviors of suspended, crossed nanotube devices made from SWNT ropes (~50 nm in diameter), with junction gap ~150 nm by mechanical manipulation under an optical microscope. The resistances of the OFF state of the devices were found consistently 10-fold larger than the ON state.

In the integrated system, electrical contacts are made only at one end of each of the lower and upper sets of nanoscale wires in the crossbar array, and thus, many device elements can be addressed from a limited number of contacts (see Fig. 6(B)). This approach suggests a highly integrated, fast, and macroscopically addressable NRAM structure that could overcome the fundamental limitations of semiconductor random access memory in

size, speed, and cost. Integration levels as high as 1×10^{12} elements per square centimeter and switching time down to ~5 ps (200-GHz operation frequency) using 5-nm device elements and 5-nm supports are envisioned while maintaining the addressability of many devices through the long (~10-μm) SWNT wires. However, such small dimensions, in particular, the junction gap size, impose significant challenges in the nanofabrication of parallel device arrays.

2.4.1.2. Nanotweezers There are two types of carbon nanotube–based nanotweezers reported by Kim and Lieber in 1999 [7] and Akita et al. in 2001 [8], respectively. Both nanotweezers employ MWNTs as tweezers' arms that are actuated by electrostatic forces. The applications of these nanotweezers include the manipulation of nanostructures and two-tip STM or atomic force microscope (AFM) probes [7].

The fabrication process of the carbon nanotube–based nanotweezers reported by Kim and Lieber [7] is illustrated in Fig. 7(A). Freestanding electrically independent electrodes were deposited onto tapered glass micropipettes with end diameters of 100 nm (Fig. 7(B)). MWNT or SWNT bundles with diameters 20–50 nm were attached to the two gold electrodes, under the direct view of an optical microscope operated in dark-field mode, using an adhesive [63, 64]. A SEM image of fabricated nanotube tweezers is shown in Fig. 7(C).

The electromechanical response of nanotube nanotweezers was investigated by applying bias voltages to the electrodes while simultaneously imaging the nanotube displacements under an optical microscope in dark-field mode. As the bias voltage increased from 0 to 8.3 V (see Fig. 8), the free ends of the tweezers' arms bent closer to each other from their relaxed position (at 0 V). The tweezers' arms relaxed to the original position when the applied voltage was removed, and this process could be repeated more than 10 times, producing the same displacement each time within the optical microscope resolution limit. These results demonstrated that the mechanical response was elastic and thus that neither the nanotubes nor the nanotube-electrode junctions deform inelastically. At 8.3 V, the distance between the tweezers' ends decreased by about 50% of the initial value, and as the voltage was increased further to 8.5 V, the tweezers' arms suddenly closed (Fig. 8(E)).

The nanotube nanotweezers have been demonstrated successfully to manipulate nanostructures, such as fluorescently labeled polystyrene spheres and β-SiC nanocluster (see Fig. 9) and GaAs nanowires [7].

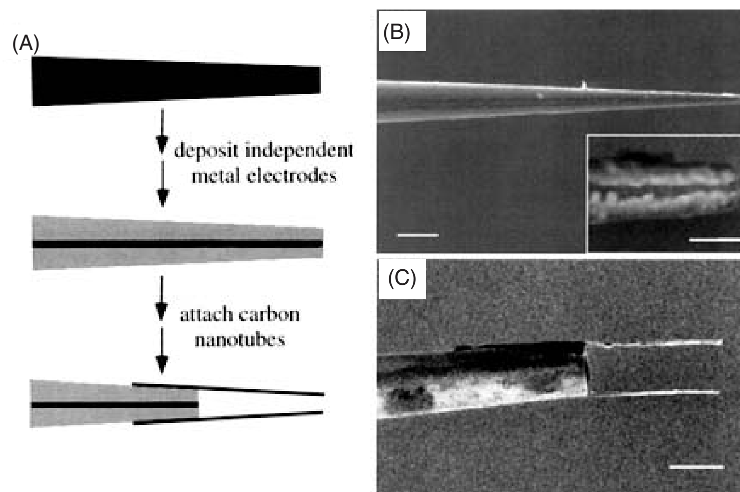

Figure 7. Overview of the fabrication process of carbon nanotube nanotweezers. (A) Schematic illustrating the deposition of two independent metal electrodes and the subsequent attachment of carbon nanotubes to these electrodes. (B) SEM image of the end of a tapered glass structure after the two deposition steps. Scale bar, 1 μm. The higher-resolution inset shows clearly that the electrodes are separated. Scale bar, 200 nm. (C) SEM image of nanotweezers after mounting two MWNT bundles on each electrode. Scale bar, 2 μm. Reprinted with permission from [7], P. Kim and C. M. Lieber, *Science* 126, 2148 (1999). © 1999, American Association for the Advancement of Science.

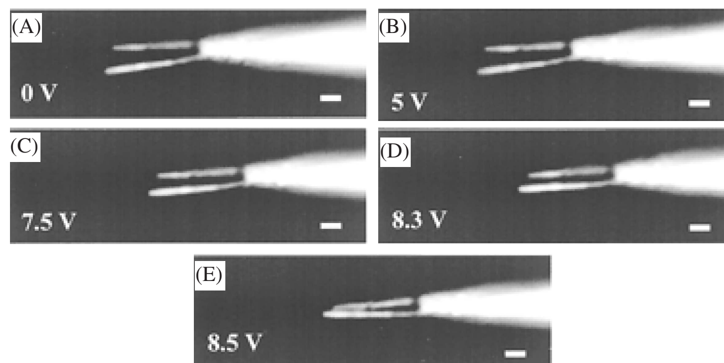

Figure 8. Dark-field-optical micrographs of electromechanical response of the nanotube nanotweezers with respect to different applied voltages. The scale bar is 1 μm. Reprinted with permission from [7], P. Kim and C. M. Lieber, *Science* 126, 2148 (1999). © 1999, American Association for the Advancement of Science.

The carbon nanotube–based nanotweezers, reported by Akita et al. [8], are shown in Fig. 10. Commercially available Si AFM cantilevers were employed as the device body. A Ti/Pt film was coated on the tip of the cantilever and connected to three Al interconnects that were patterned on the cantilever by a conventional lithographic technique as shown in Fig. 10(A). The Ti/Pt film was separated into two by focused ion beam etching. These two parts were independently connected to Al interconnects as shown in Fig. 10(B). DC voltage was applied between the separated Ti/Pt tips, through the Al interconnects, to operate the tweezers after attaching two arms of nanotubes on them.

The attachment of the nanotubes was carried out in a specially designed field-emission-type SEM with three independent movable stages. The Si cantilever and the nanotube cartridge were mounted on two different stages. A third stage, where a tungsten needle was installed, was used for the fine adjustment of the position of the nanotubes after being mounted to the Si tip. When the metal-coated Si tip was manipulated to be in contact with a target nanotube, an amorphous carbon film was deposited on this contact portion by the electron-beam dissociation of contaminants, mainly hydrocarbons, in the SEM chamber. The target nanotube was finally pulled away from the cartridge. Another nanotube was also attached in the same manner. The position of the two nanotube arms was adjusted to be parallel by using the stage with the tungsten needle and fixed by deposition of the carbon films at the base of the arms. The nanotube arms were also coated with an ultrathin carbon film (a few to several nanometers) to achieve insulation from the outside. This film coating prevents large current flows when the two nanotube arms close or pick up a conductive particle. Figure 11(a) shows a SEM image of a typical pair of nanotube nanotweezers prepared this way. Two arms of the nanotubes were fixed at the most appropriate position on the Si tips. Their length was 2.5 μm, and the separation between their tips was 780 nm.

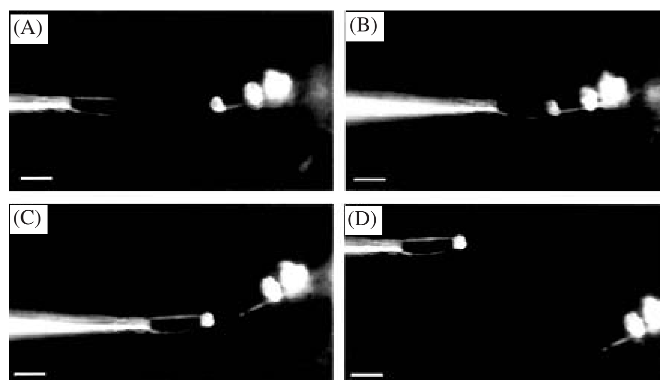

Figure 9. Dark-field-optical micrographs showing the sequential process of nanotweezer manipulation of polystyrene nanoclusters containing fluorescent dye molecules. Reprinted with permission from [7], P. Kim and C. M. Lieber, *Science* 126, 2148 (1999). © 1999, American Association for the Advancement of Science.

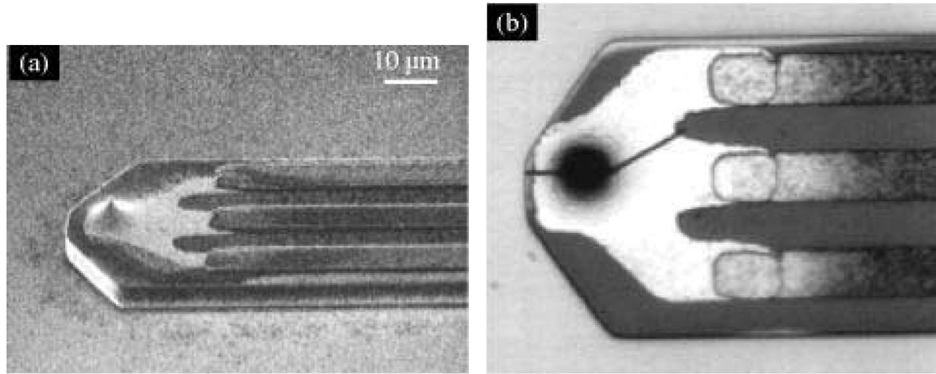

Figure 10. SEM images of a Si cantilever as a base for nanotube nanotweezers. (a) A Ti/Pt film was coated on the tip and connected to three Al lines patterned on the cantilever. (b) The Ti/Pt film was separated into two by a focused ion beam, and these two were connected to the one and two Al lines, respectively. Reprinted with permission from [8], S. Akita et al., *Appl. Phys. Lett.* 79, 1691 (2001). © 2001, American Institute of Physics.

The operation of the nanotube nanotweezers was examined by *in situ* SEM. Various voltages were applied between the two arms to get them to close because of the electrostatic attraction force. Figures 11(b)–7(d) show the motion of the nanotube arms as a function of the applied voltage V. It is clearly seen that the arms bent and the separation between the tips decreased with increasing applied voltage. The separation became 500 nm at $V = 4$ V and zero at $V > 4.5$ V. It is noted that the motion in Figs. 11(a)–11(d) could be repeated many times without any permanent deformation, showing that carbon nanotubes are ideal materials for building NEMS.

2.4.1.3. Rotational Motors A carbon nanotube–based rotational motor, reported by Fennimore et al. in 2003 [9], is conceptually illustrated in Fig. 12(a). The rotational element (R), a solid rectangular metal plate serving as a rotor, is attached transversely to a suspended support shaft. The support shaft ends are embedded in electrically conducting anchors (A1, A2) that rest on the oxidized surface of a silicon chip. The rotor plate assembly is surrounded

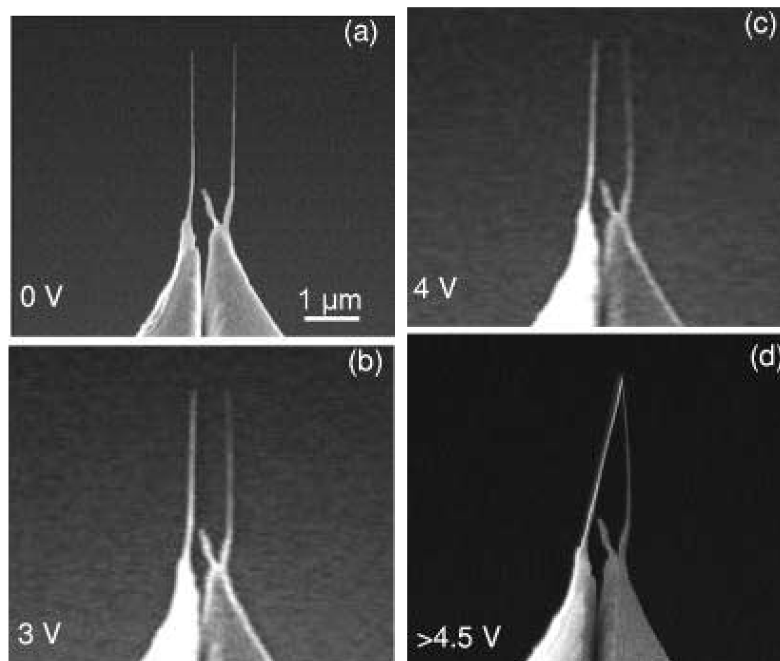

Figure 11. SEM images of the motion of nanotube arms in a pair of nanotweezers as a function of the applied voltage. Reprinted with permission from [8], S. Akita et al., *Appl. Phys. Lett.* 79, 1691 (2001). © 2001, American Institute of Physics.

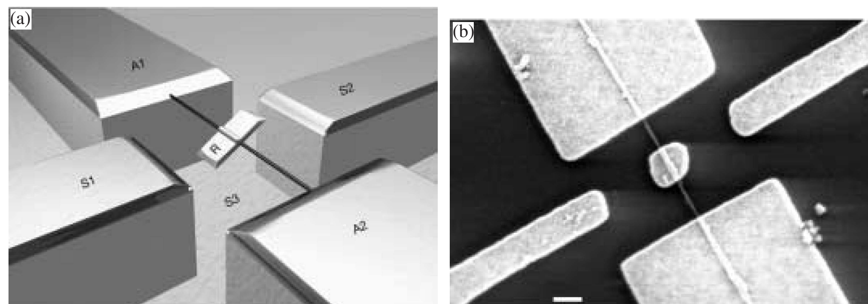

Figure 12. Integrated synthetic nanoelectromechanical systems (NEMS) actuator. (a) Conceptual drawing of nanoactuator. (b) SEM image of nanoactuator just prior to HF etching. Scale bar, 300 nm. Reprinted with permission from [9], A. M. Fennimore et al., *Nature* 424, 408 (2003). © 2003, Nature Publishing Group.

by three fixed stator electrodes: two "in-plane" stators (S1, S2) are horizontally opposed and rest on the silicon oxide surface, and the third "gate" stator (S3) is buried beneath the surface. Four independent (DC and/or appropriately phased AC) voltage signals, one to the rotor plate and three to the stators, are applied to control the position, speed, and direction of rotation of the rotor plate. The key component in the assembly is a MWNT, which serves simultaneously as the rotor plate support shaft and the electrical feed-through to the rotor plate; most importantly, it is also the source of rotational freedom.

The nanoactuator was constructed using lithographic methods. MWNTs in suspension were deposited on a doped silicon substrate covered with 1 μm of SiO_2. The nanotubes were located using an AFM or a SEM. The remaining actuator components (in-plane rotor plate, in-plane stators, anchors, and electrical leads) were then patterned using electron-beam lithography. An HF etch was used to remove roughly 500 nm of the SiO_2 surface to provide clearance for the rotor plate. The conducting Si substrate here serves as the gate stator. Figure 12(b) shows an actuator device prior to etching. Typical rotor plate dimensions were 250–500 nm on a side.

The performance of the nanoactuator was examined *in situ* inside the SEM chamber. Visible rotation could be obtained by applying DC voltages up to 50 V between the rotor plate and the gate stator. When the applied voltage was removed, the rotor plate would rapidly return to its original horizontal position. To exploit the intrinsic low-friction-bearing behavior afforded by the perfectly nested shells of MWNTs, the MWNT supporting shaft was modified *in situ* by successive application of very large stator voltages. The process resulted in fatigue and eventually shear failure of the outer nanotube shells. In the "free" state, the rotor plate was still held in position axially by the intact nanotube core shells but could be azimuthally positioned, using an appropriate combination of stator signals, to any arbitrary angle between 0° and 360°. Figure 13 shows a series of still SEM images, recorded from an actuated device in the free state, being "walked" through one complete rotor plate revolution using quasi-static DC stator voltages. The stator voltages were adjusted sequentially to attract the rotor plate edge to successive stators. By reversing the stator voltage sequence, the rotor plate rotation could be reversed in an equally controlled fashion. Finite frequency operation of the actuator was also performed using a variety of suitably phased AC and DC voltage signals to the three stators and rotor plate. The rotor plate was successfully flipped between the extreme horizontal (90° and 270°) positions. The experiments show that the MWNT clearly serves as a reliable, presumably wear-free, NEMS element providing rotational freedom. No apparent wear or degradation in performance was observed after many thousands of cycles of rotations.

The potential applications of the MWNT-based actuators include ultra-high-density optical sweeping and switching elements, paddles for inducing and/or detecting fluid motion in microfluidics systems, gated catalysts in wet chemistry reactions, biomechanical elements in biological systems, or general (potentially chemically functionalized) sensor elements.

2.4.1.4. Nanorelays Carbon nanotube–based nanorelays were first reported by Kinaret et al. in 2003 [10] and later experimentally demonstrated by Lee et al. in 2004 [41]. The nanorelay is a three-terminal device including a conducting carbon nanotube placed on a

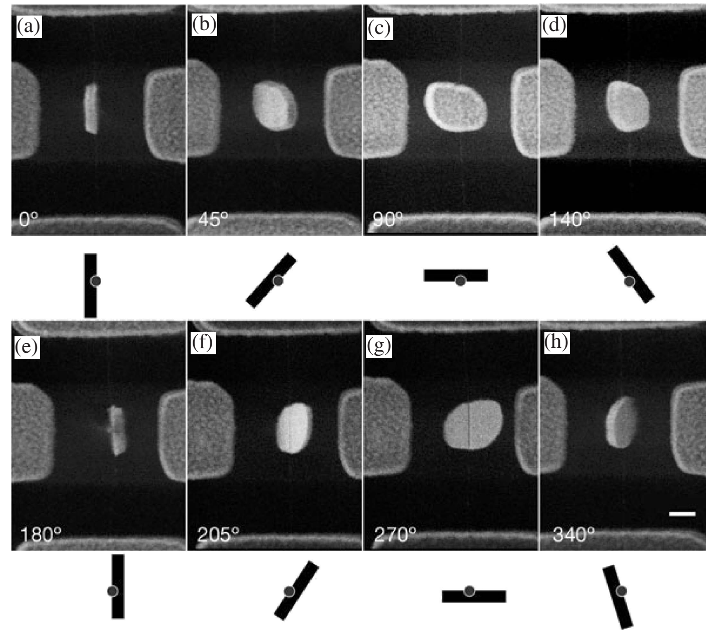

Figure 13. Series of SEM images showing the actuator rotor plate at different angular displacements. The schematic diagrams located beneath each SEM image illustrate a cross-sectional view of the position of the nanotube/rotor-plate assembly. Scale bar, 300 nm. Reprinted with permission from [9], A. M. Fennimore et al., *Nature* 424, 408 (2003). © 2003, Nature Publishing Group.

terrace in a silicon substrate and connected to a fixed-source electrode (S), as shown in Fig. 14(A). A gate electrode (G) is positioned underneath the nanotube so that a charge can be induced in the nanotube by applying a gate voltage. The resulting capacitance force q between the nanotube and the gate bends the tube and brings the tube end into contact with a drain electrode (D) on the lower terrace, thereby closing an electric circuit. Theoretical modeling of the device shows that there is a sharp transition from a nonconducting (OFF) to a conducting (ON) state when the gate voltage is varied at a fixed source-drain voltage. The sharp switching curve allows for amplification of weak signals superimposed on the gate voltage [10].

One fabricated nanorelay device is shown in Fig. 14(B). A multiwalled nanotube was positioned on top of the source, gate, and drain electrodes with PMMA as sacrificial layer using AC-electrophoresis techniques [34]. Then, a top electrode was placed over the nanotube at the source to ensure good contact. The underlying PMMA layer was then carefully removed to produce a nanotube suspended over the gate and drain electrodes. The separation between gate and drain was approximately 250 nm, and the source drain distance was 1.5 μm.

The electromechanical properties of nanotube relays were investigated by measuring the current-gate voltage (I–V_{sg}) characteristics, while applying a source-drain voltage of 0.5 V. Figure 15 shows the I–V_{sg} characteristics of one of the nanotube relays with an initial height

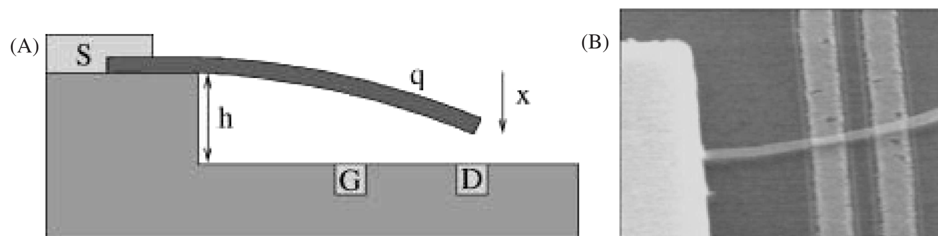

Figure 14. Schematic diagrams of a CNT nanorelay device (A). Reprinted with permission from [10], J. Kinaret et al., *Appl. Phys. Lett.* 82, 1287 (2002). © 2002, American Institute of Physics. SEM image of a fabricated nanorelay device (B). Reprinted with permission from [41], S. Lee et al., *Nano Lett.* 4, 2027 (2004). © 2004, American Chemical Society.

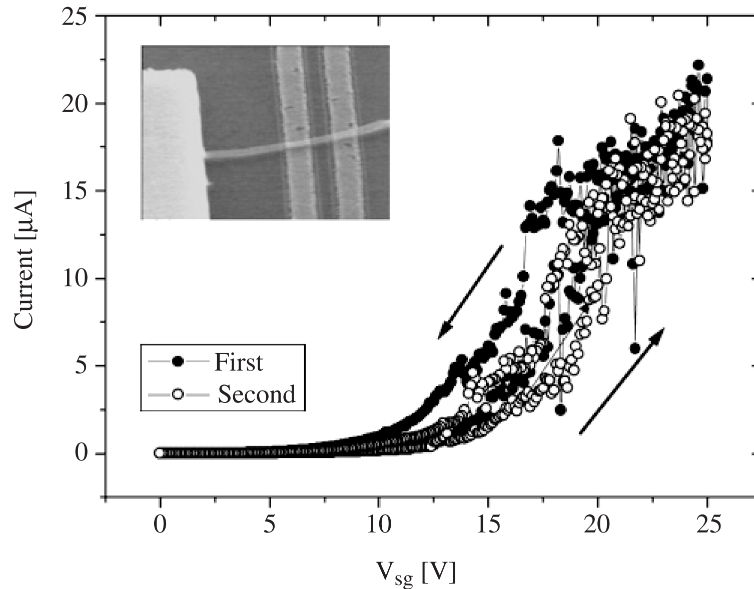

Figure 15. I–V_{sg} characteristics of a nanotube relay initially suspended approximately 80 nm above the gate and drain electrodes. Reprinted with permission from [41], S. Lee et al., *Nano Lett.* 4, 2027 (2004). © 2004, American Chemical Society.

difference between the nanotube and drain electrode of approximately 80 nm. The drain current started to increase nonlinearly when the gate voltage reached 3 V (at this gate voltage, the current is on the order of 10 nA). The nonlinear current increase was a signature of electron tunneling as the distance between the nanotube and the drain electrode was decreased. Beyond $V_{sg} = 20$ V, there was a change in the rate of current increase. With the current increase rate becoming more linear, strong fluctuations could be detected. The deflection of the nanotube was found to be reversible. The current decreased with the reduction of gate voltage, showing some hysteresis, until it reached zero for a gate voltage below 3 V. The current measured during the increasing V_{sg} part of the second scan closely followed that of the first scan, especially in the region below $V_{sg} = 12$ V.

The dynamics of nanorelays was recently investigated by Jonsson et al. [65]. The results show that the intrinsic mechanical frequencies of nanorelays are in the gigahertz regime, and the resonance frequency can be tuned by the biased voltage.

The potential applications of nanorelays include memory elements, pulse generators, signal amplifiers, and logic devices.

2.4.1.5. Feedback-Controlled Nanocantilevers A feedback-controlled carbon nanotube–based NEMS devices reported by Ke and Espinosa 2004 [11], schematically shown in Fig. 16, is made of a multiwalled carbon nanotube placed as a cantilever over a microfabricated step. A bottom electrode, a resistor, and a power supply are parts of the device circuit.

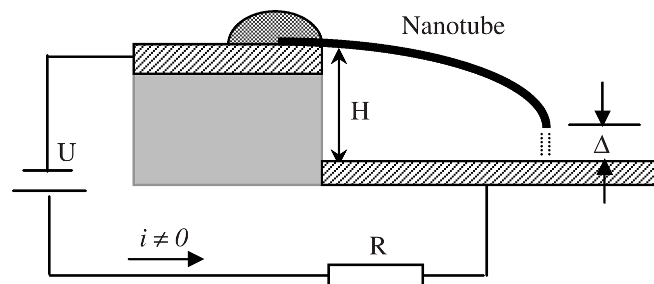

Figure 16. Schematic of nanotube-based device with tunneling contacts. Reprinted with permission from [11], C.-H. Ke and H. D. Espinosa, *Appl. Phys. Lett.* 85, 681 (2004). © 2004, American Institute of Physics.

When the applied voltage U < V_{PI} (pull-in voltage), the electrostatic force is balanced by the elastic force from the deflection of the nanotube cantilever. The nanotube cantilever remains in the "upper" equilibrium position. When the applied voltage exceeds a pull-in voltage, the electrostatic force becomes larger than the elastic force and the nanotube accelerates toward the bottom electrode. When the tip of the nanotube is very close to the electrode (i.e., gap $\Delta \approx 0.7$ nm) as shown in Fig. 16, a substantial tunneling current passes between the tip of the nanotube and the bottom electrode. Because of the existence of the resistor R in the circuit, the voltage applied to the nanotube drops, weakening the electric field. Because of the kinetic energy of the nanotube, it continues to deflect downward, and the tunneling current increases, weakening the electric field further. In this case, the elastic force is larger than the electrostatic force, and the nanotube decelerates and eventually changes the direction of motion. This decreases the tunneling current and the electrical field recovers. If there is damping in the system, the kinetic energy of the nanotube is dissipated and the nanotube stays at the position where the electrostatic force is equal to the elastic force, and a stable tunneling current is established in the device. This is the "lower" equilibrium position for the nanotube cantilever. At this point, if the applied voltage U decreases, the cantilever starts retracting. When U decreases to a certain value, called pull-out voltage V_{PO}, the cantilever is released from its lower equilibrium position and returns back to its upper equilibrium position. At the same time, the current in the device diminishes substantially. Basically, the pull-in and pull-out processes follow a hysteretic loop for the applied voltage and the current in the device. The upper and lower equilibrium positions correspond to ON and OFF states of a switch, respectively. Also the existence of the tunneling current and feedback resistor make the "lower" equilibrium states very robust, which is key to some applications of interest. The representative characteristic curve of the device is shown in Fig. 17: (a) shows the relation between the gap Δ and the applied voltage U; (b) shows the relation between the current i in the circuit and the applied voltage U.

The current jump behavior at the pull-in has been observed for a nanotube cantilever freestanding above an electrode actuated by electrostatic forces [32], as shown in Fig. 18, and the I–V behavior after the pull-in has been demonstrated based on the good agreement between experimental measurements and theoretical prediction. The parameters used in the theoretical prediction includes the length of the nanotube $L = 3.8$ μm; the diameter of the nanotube $R_{ext} = 20$ nm; and the initial gap between the nanotube cantilever and the electrode $H = 200$ nm, $R = 0.98$ GΩ, and contact resistance $R_0 = 50$ Ω [11].

The potential applications of the device include ultrasonic wave detection for monitoring the health of materials and structures, gap sensing, NEMS switches, memory elements, and logic devices.

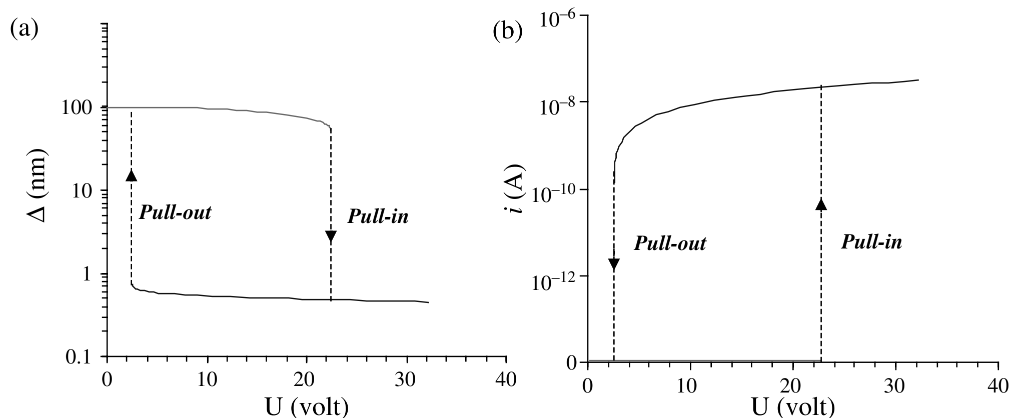

Figure 17. Representative characteristic of pull-in and pull-out processes for the feedback-controlled nanocantilever device. (a) Relationship between the gap Δ and the applied voltage U. (b) Relationship between the current i in the circuit and the applied voltage U. Reprinted with permission from [11], C.-H. Ke and H. D. Espinosa, *Appl. Phys. Lett.* 85, 681 (2004). © 2004, American Institute of Physics.

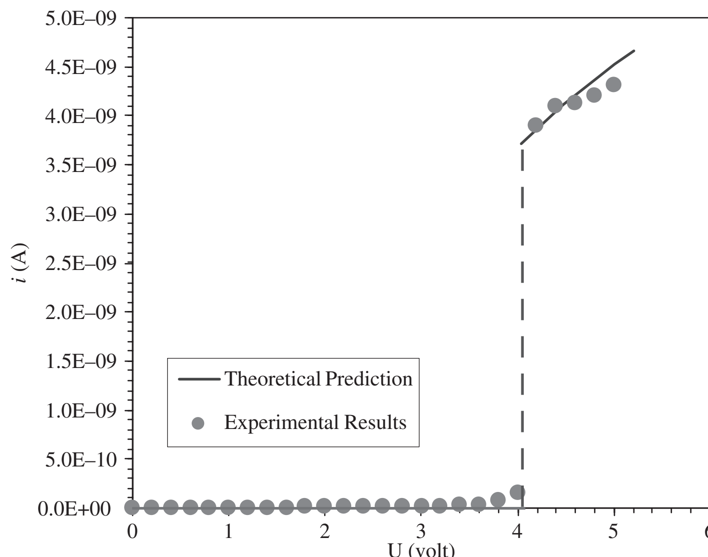

Figure 18. Comparison between theoretical prediction and I–V measurement of an electrostatically actuated free-standing nanotube cantilever with an electronic circuit incorporating a resistor.

In comparison to nanorelays [10, 41], the device reported in Ref. [11] is a two-terminal device, providing more flexibility in terms of device realization and control than the nano-relay. In comparison to the NRAM described in Ref. [1], the feedback-controlled device employs an electrical circuit incorporated with a resistor to adjust the electrostatic field to achieve the second stable equilibrium position. This feature reduces the constraints in fabricating devices with nanometer gap control between the freestanding CNTs or NWs and the substrate, providing more reliability and tolerance to variability in fabrication parameters. However, the drawback of the device in memory applications is that the memory becomes volatile. The working principle and the potential applications for these two devices are somewhat complementary.

2.4.1.6. Tunable Oscillators The fabrication and testing of a tunable carbon nanotube oscillator was reported by Satonova et al. [12]. It consists of a doubly clamped nanotube, as shown in Fig. 19. They demonstrated that the resonance frequency of the oscillators can be widely tuned and that the devices can be used to transduce very small forces.

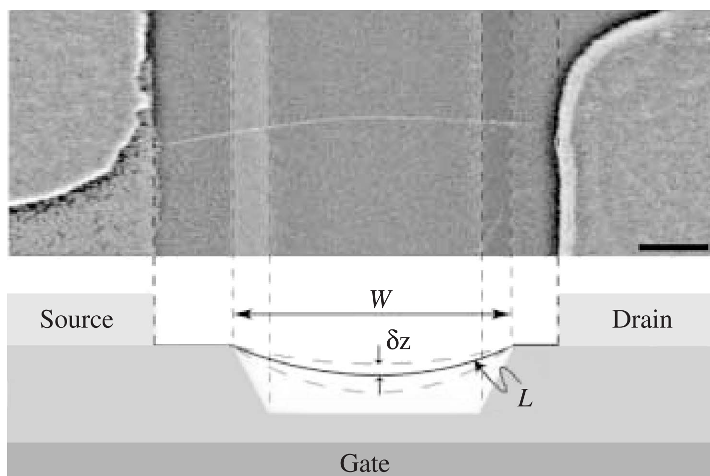

Figure 19. SEM image of a suspended device (top) and a schematic of device geometry (bottom). Scale bar, 300 nm. The sides of the trench, typically 1.2–1.5 μm wide and 500 nm deep, are marked with dashed lines. A suspended nanotube can be seen bridging the trench. Reprinted with permission from [12], V. Sazonova et al., *Nature* 431, 284 (2004). © 2004, Nature Publishing Group.

Single- or few-walled nanotubes with diameters in the range of 1–4 nm, grown by CVD were suspended over a trench (typically 1.2–1.5 μm wide, 500 nm deep) between two metal (Au/Cr) electrodes. A small section of the tube resided on the oxide on both sides of the trench; the adhesion of the nanotube to the oxide provided clamping at the end points. The nanotube motion was induced and detected using the electrostatic interaction with the gate electrode underneath the tube. In this device, the gate voltage has both a static (DC) component and a small time-varying (AC) component. The DC voltage at the gate produces a static force on the nanotube that can be used to control its tension. The AC voltage produces a periodic electric force, which sets the nanotube into motion. As the driving frequency approaches the resonance frequency of the tube, the displacement becomes large.

The transistor properties of semiconducting [66] and small-bandgap semiconducting [67, 68] carbon nanotubes were employed to detect the vibrational motion. Figure 20(a) shows the measured current through the nanotube as a function of driving frequency at room temperature. A distinctive feature in the current on top of a slowly changing background can be seen. This feature is due to the resonant motion of the nanotube, which modulates the capacitance, while the background is due to the modulating gate voltage.

The DC voltage on the gate can be used to tune the tension in the nanotube and therefore the oscillation frequency. Figure 20(b) and 20(c) show the measured response as a function of the driving frequency and the static gate voltage. The resonant frequency shifts upward as the magnitude of the DC gate voltage is increased. Several distinct resonances are observed, corresponding to different vibrational modes of the nanotube. Figure 20(d) shows the theoretical predictions for the dependence of the vibration frequency on gate voltage for a representative device. The predictions are based on finite element analysis, with the nanotube modeled as a long beam suspended over a trench. With the increase of the gap voltage, the deflection of the nanotube becomes larger and the stretching dominates the bending. Therefore, the stiffness of the nanotube beam increases and so does the resonance frequency. The theoretical predictions (Fig. 20(d)) show good qualitative agreement with experiments (Fig. 20(b) and 20(c)). The device showed a high-force sensitivity (below 5aN), which made it a small-force transducer.

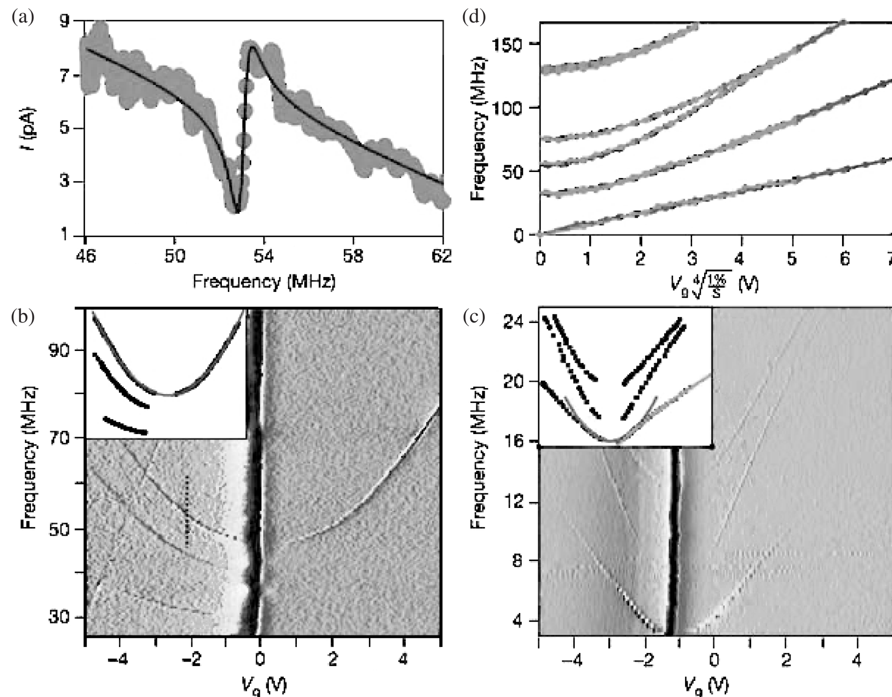

Figure 20. Measurements of resonant response. (a) Detected current as a function of driving frequency. (b)–(c) Detected current as a function of gate voltage V_g and frequency for devices 1 and 2. (d) Theoretical predictions for the dependence of vibration frequency on gate voltage for a representative device. Reprinted with permission from [12], V. Sazonova et al., *Nature* 431, 284 (2004). © 2004, Nature Publishing Group.

2.4.2. Nanowire-Based Nanoelectromechanical Systems Devices

Nanowires, like carbon nanotubes, are high-aspect-ratio, one-dimensional nanostructures. The materials of nanowires include silicon [52, 69–72], gold [73, 74], silver [75–77], platinum [24], germanium [71, 78–81], zinc oxide [82, 83], and so on. Besides their size, the advantages offered by nanowires when employed in NEMS are their electronic properties, which can be controlled in a predictable manner during synthesis. This has not been achieved yet for carbon nanotubes. In contrast to carbon nanotubes, nanowires do not exhibit the same degree of flexibility, which may be a factor concerning device fabrication and reliability. In the following section, two nanowire-based NEMS device are briefly reviewed.

2.4.2.1. Resonators Figure 21 shows a suspended platinum nanowire resonator (a), reported by Husain et al. 2003 [24], and the circuit used for magnetomotive drive and detection of its motion (b).

Synthetized platinum nanowires were deposited on a Si substrate capped by a 300-nm-thick layer of thermally grown silicon dioxide and prepatterned with Au alignment marks. The location of the deposited wires was mapped, by means of optical microscopy, using their strong light-scattering properties [76, 84]. Metallic leads (5 nm Cr, 50 nm Au) to individual wires were subsequently patterned by electron-beam lithography, evaporation, and lift-off. Finally, the SiO_2 was removed by wet etching (HF) to form suspended nanowire structures. The suspended Pt nanowire shown in Fig. 21 has a diameter of 43 nm and a length of 1.3 μm. A magnetomotive detection scheme (see Fig. 21, right), in which an AC current drives a beam in a transverse magnetic field, was used to drive and read out the resonators. Figure 22 shows the measured motion-induced impedance of the nanowire device, $|Z_m(f)|$, versus frequency. The measured quality factor Q was approximately 8500 and decreased slightly with the increase in magnetic field. It was noted that the characteristic curve shown in Fig. 22 corresponds to a linear response of the beam. Badzey et al. [52] reported a doubly clamped nanomechanical Si beam working in the nonlinear response region. The nonlinear response of the beam displays notable hysteresis and bistability in the amplitude-frequency space when the frequency sweeps upward and downward. This particular behavior shows that the device can be used as mechanical memory elements.

2.4.2.2. Nanoelectromechanical Programmable Ready-Only Memory A nanowire-based nanoelectromechanical programmable read-only memory (NEMPROM), reported by Ziegler et al. 2004 [80], is shown in Fig. 23(a). The germanium nanowire was synthesized directly onto a macroscopic gold wire (diameter = 0.25 mm). The combination of TEM and STM was used to control and visualize the nanowire under investigation. Figure 23(b)–23(g) illustrates how the device can work as NEMPROM. In equilibrium, the attractive van der Waals (vdW) force and electrostatic interactions between the nanowire and the gold electrode are countered by the elastic force from the deflection of the nanowire. Figure 23(b) shows the position of the nanowire with relative low applied voltage. With the increase in voltage, the nanowire moves closer to the electrode (Fig. 23(c)). When the applied voltage exceeds a certain value, a jump-to-contact happens, i.e., the nanowire makes physical contact with the electrode (Fig. 23(d)). The nanowire remains in contact with the electrode even when the electrostatic field is removed because the vdW force is larger than the elastic force (Fig. 23(e)). This is the ON state of the NEMPROM. The NEMPROM device

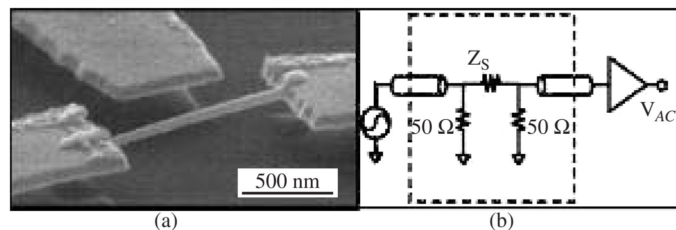

Figure 21. (a) SEM image of the suspended nanowire device, 1.3 μm long and 43 nm in diameter. (b) Measurement circuit used for magnetomotive drive and detection. Reprinted with permission from [24], A. Husain et al., *Appl. Phys. Lett.* 83, 1240 (2003). © 2003, American Institute of Physics.

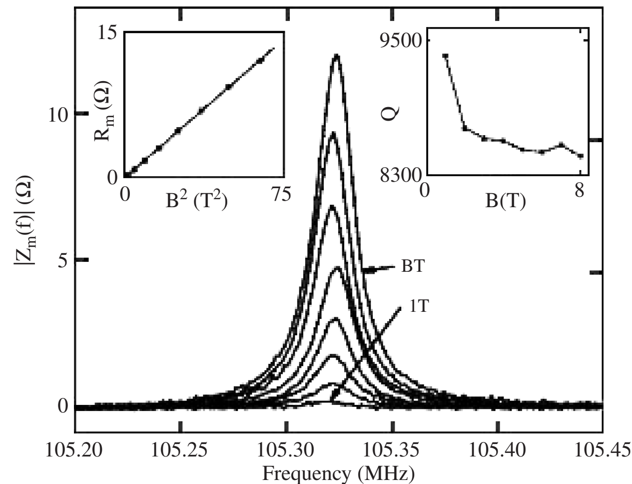

Figure 22. Measured mechanical impedance of a Pt nanowire device as a function of frequency, at a series of magnetic fields from 1 to 8 T. The left inset shows the characteristic B^2 dependence typical of magnetomotive detection. The right inset shows the quality factor Q as a function of magnetic field. Reprinted with permission from [24], A. Husain et al., *Appl. Phys. Lett.* 83, 1240 (2003). © 2003, American Institute of Physics.

can be switched OFF by mechanical motion or by heating the device above the stability limit to overcome the vdW attractive forces. Figure 23(f) and 23(g) show the separation of the nanowire and the electrode after imposing a slight mechanical motion, resulting in a jump-off-contact event. This is the OFF state of NEMPROM. The working principle of NEMPROM is similar to that of NRAM [1] since both of them employ van der Waals energy to achieve the bistability behavior, although the usage of germanium may provide better control of size and electrical behaviors of the device than that of carbon nanotube.

2.5. Future Challenges

NEMS offer unprecedented and intriguing properties in the fields of sensing and electronic computing. Although significant advancement has been achieved, there are many challenges that will need to be overcome before NEMS can replace and revolutionize current

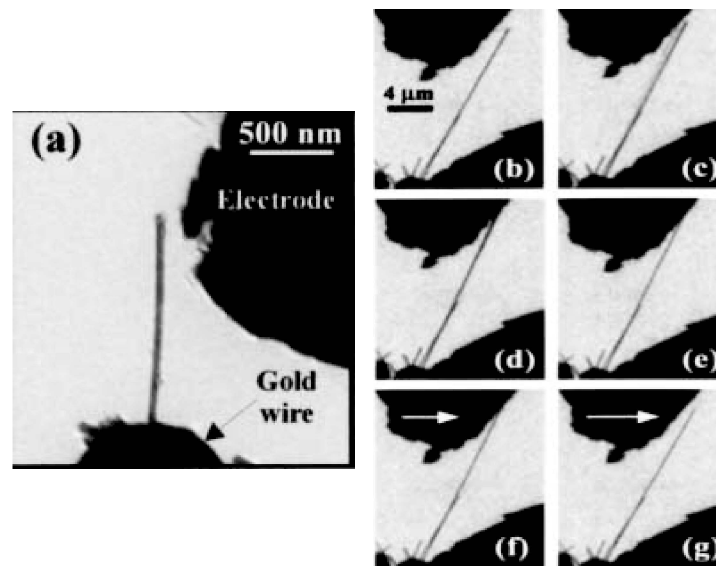

Figure 23. (a) TEM image of a Ge nanowire device. (b)–(d) TEM sequence showing the jump-to-contact of a Ge nanowire as the voltage is increased. (e) TEM image demonstrating the stability of device after removal of the electrostatic potential. (f) and (g) TEM sequence demonstrating the resetting behavior of the device. Reprinted with permission from [80], K. J. Ziegler et al., *Appl. Phys. Lett.* 84, 4074 (2004). © 2004, American Institute of Physics.

technologies. Among the issues that need further research and development are

1. *Extremely high integration level*: For applications such as RAM and data storage, the density of the active components is definitely a key parameter. Direct growth and directed self-assembly are the two most promising methods to make NEMS devices with levels of integration orders of magnitudes higher than that of current microelectronics.

   A process for nanofabrication of the NEMS device developed by Ke and Espinosa [11], based on the directed self-assembly, is schematically shown in Fig 24.

   a. A 1-μm-thick Si_3N_4 dielectric film is deposited on a Si wafer by LPCVD. Then, a 50-nm-thick gold film (with 5 nm Cr film as adhesion layer) is deposited by e-beam evaporation and patterned by lithography to form the bottom electrodes. A 1-μm-thick SiO_2 layer is deposited by PECVD.
   b. The fountain-pen nanolithography technique [85] is then employed to functionalize specific areas, with widths down to 40 nm, either with polar chemical groups (such as the amino groups ($-NH_2/-NH_3^+$) of cysteamine) or carboxyl ($-COOH/-COO^-$) or with nonpolar groups (such as methyl ($-CH_3$) from molecules like 1-octadecanethiol, ODT).
   c. The substrate is dipped into a solution containing prefunctionalized (with polar chemical groups) CNTs or NWs to adhere and self-assembly to the functionalized sites.
   d. The chip is patterned with e-beam lithography and e-beam evaporation of 100 nm gold film (lift-off, with 5 nm Cr film as adhesion layer) to form the top electrodes.
   e. Removal of the SiO_2 layer using wet etching (HF) to free one end of the CNT cantilever completes the process.

   The final product, a two-dimensional array of NEMS devices, with multiplexing capabilities is schematically shown in Fig. 25. The top and bottom electrodes are interconnected to the pads, correspondingly. By applying voltage between the corresponding pads, the individual NEMS devices can be independently actuated.
2. *Better understanding the quality factor*: One of the keys to realize the potential applications of NEMS is to achieve ultra-high-quality factors. However, it has been consistently observed that the quality factor of resonators decreases significantly with size scaling [5]. Defects in the bulk materials and interfaces, fabrication-induced surface damages, adsorbates on the surface, and thermoelastic damping are a few commonly listed factors that can dampen the motion of resonators. Unfortunately, the dominant energy dissipation mechanism in nanoscale mechanical resonators is still unclear.
3. *Reproducible and routine nanomanufacturing*: Fabrication reproducibility is key in applications such as mass sensors. Because the NEMS can respond to mass at the level of single atom or molecules, it places an extremely stringent requirement on the cleanness and precision of nanofabrication techniques. Likewise, devices that rely on van der Waals energy require dimensional control (e.g., gap dimension) in the order of a few nanometers.

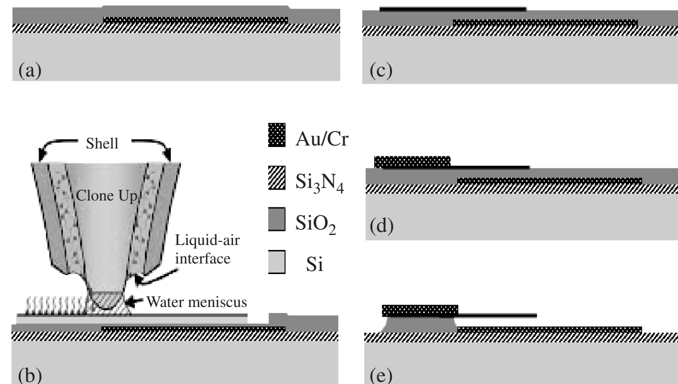

Figure 24. Schematic of the fabrication steps involving NFP functionalization.

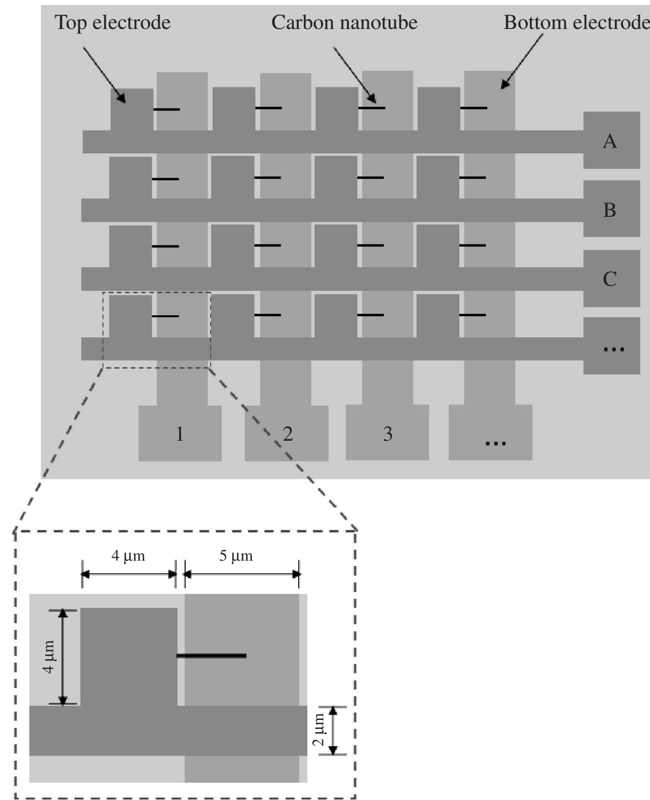

Figure 25. Schematics of two-dimensional array of the NEMS device with multiplexing.

4. *Quantum limit for mechanical devices*: The ultimate limit for NEMS is its operation at, or even beyond, the quantum limit [5]. In the quantum regime the individual mechanical quanta are of the same order of magnitude, or greater than the thermal energy. Quantum theory should be used to understand and optimize force and displacement measurements. Recently, position resolution with a factor of 4.3 above the quantum limit has been achieved for a single-electron transistor with high-quality factor at millikelvin temperature [86]. The pursuit of NEMS devices operating at the quantum limit will potentially open new fields in science at the molecular level.

3. MODELING OF NANOELECTROMECHANICAL SYSTEMS DEVICES

The design of NEMS depends on a thorough understanding of the mechanics of the devices themselves and the interactions between the devices and the external forces/fields. With the critical dimension shrinking from micron to nanometer scale, new physics emerges so that the theory typically applied to MEMS does not immediately translated to NEMS. For example, van der Waals forces from atomic interactions play an important role in NEMS, while they can be generally neglected in MEMS. The behavior of materials at nanometer scale begins to be atomistic rather than continuous, giving rise to anomalous and often nonlinear effects, for example,

- The roles of surfaces and defects become more dominant.
- The devices become more compliant than continuum models predict.
- Molecular interactions and quantum effects become key issues to the point that thermal fluctuation could make a major difference in the operation of NEMS.

For instance, the nanoresonators reported by the research groups of Roukes and Craighead are operated in the gigahertz range and usually have sizes within $200 \times 20 \times 10$ nm^3 [87]. Devices of this size and smaller are so minuscule that material defects and surface effects have a large impact on their performance.

In principle, atomic-scale simulations should well predict the behavior of NEMS devices. However, atomic simulations of the entire NEMS involve prohibitively expensive computational resources or exceed the current computational power. Alternatively, multiscale modeling, which simulates the key region of a device with an atomistic model and other regions with a continuum model, can well serve the purpose under the circumstance of limited computational resources. Besides, it has been demonstrated that the behavior of some nanostructures, like carbon nanotubes, can be approximated by continuum mechanics models, based on the same potentials governing molecular dynamics (MD) simulation [88], if the surface nonideality of the nanostructures is neglected. Thus, continuum mechanics models are still adequate to the design of NEMS, in particular, in the initial stages.

3.1. Multiscale Modeling

Multistage modeling can be pursued sequentially or concurrently. In the sequential method, information from each model at a given scale is passed to the next modeling level. In this fashion, "informed" or physically motivated models are developed at larger scales. In concurrent multiscale modeling, the system is split into primarily two domains: the atomistic domain and the continuum domain. In the atomistic domain, MD and quantum mechanics (QM) are typically employed, while in the continuum domain, the finite element method is often used. MD deals with the interaction of many thousands of atoms or more according to an interaction law. The "constitutive" behavior of each atom is governed by QM. QM involves the electronic structure, which in turn determines the interatomic force law—the "constitutive" behavior of each atom. However, in practice, the interatomic force laws have been determined empirically based on both QM and experiments. To model the response of NEMS devices, MD and continuum mechanics are generally adequate; hence, here we restrict our discussion to the basic ideas behind these two models. In some cases, QM modeling is required so the reader should consult the information on QM.

As an example of sequential multiscale modeling, we discuss how the mechanical properties of bulk tantalum were calculated using a multiscale modeling strategy. Moriarty et al. [89] started with fundamental atomic properties and used rigorous quantum-mechanical principles calculations to develop accurate interatomic force laws that were then applied to atomistic simulations involving many thousands of atoms. From these simulations, they derived the properties of individual dislocations in a perfect crystal and then, with a new microscale simulation technique, namely, dislocation dynamics, examined the behavior of large collections of interacting dislocations at the microscale in a grain-sized crystal. They modeled the grain interactions in detail with finite-element simulation, and from those simulations, they finally constructed appropriate models of properties such as yield strength in a macroscopic volume of tantalum. At each length scale, the models were experimentally tested and validated with available data. The concept of information passing between models, from quantum modeling to atomic to continuum scale, is quite general and can be applied in a variety of problems including NEMS.

3.1.1. Implementation of Concurrent Multiscale Modeling

MD computes the classical trajectories of atoms by integrating Newton's law, $F = ma$, for the system. In the MD domain, the interaction force follows an empirical potential. Consider a set of n_M molecules with the initial coordinates X_I, $I = 1$ to n_M. Let the displacements be denoted by $d_I(t)$. The potential energy is then given by $W_M(d)$. For a given potential function $W_M(d)$, an equilibrium state is given by

$$dW_M(d) = 0 \tag{1}$$

From the continuum viewpoint, the governing equations arise from conservation of mass, momentum and energy. Using a so-called total Lagrangian description [90], the linear momentum equations are

$$\frac{\partial P_{ji}}{\partial X_j} + \rho_0 b_i = \rho_0 \ddot{u}_i \tag{2}$$

where ρ_0 is the initial density, P is the nominal stress tensor, b is the body force per unit mass, u the displacement, and the superposed dots denote material time derivatives.

There are two approaches to building a multiscale model: domain decomposition with overlapping domains, often referred to as the “handshake” model [87], and the edge-to-edge decomposition method [91].

The main features of the overlapping domain decomposition include: (a) A Lagrange multiplier method and an augmented Lagrange method to impose consider the constraints on the motion; (b) The Lagrange multiplier field in the overlapping domain vanishes at the edges of the continuum domain so that the interaction forces between the continuum and molecular mechanics model are smooth if an atom exits the overlapping domain.

In edge-to-edge decomposition coupling method, there are three types of particles. Besides the nodes of the continuum domain and the atoms of the molecular domain, virtual atoms are defined to model the bond angle-bending for bonds between the continuum and the molecular domains. The virtual atoms are connected with the molecular domain by virtual bonds. An example showing the domains in difference of all these methods, when applied to the modeling of a graphite sheet, is shown in Fig. 26.

3.1.2. Examples of Concurrent Multiscale Modeling

Because of the computational power and efficiency, multiscale modeling has been used widely in the modeling and simulation of nanostructures and NEMS. Here three examples are highlighted: carbon nanotube fracture [91], carbon nanotube–based switch performance [88], and nanogears kinematics [87].

In the model developed by Belytschko et al. [91] for studying carbon nanotubes fracture, two shells of a nanotube interacting by van der Waals forces were considered. The molecular model was used only in a small subdomain surrounding a defect, while the finite element model was employed outside of the molecular model (Fig. 27). A modified Morse potential was used. The load was only applied to the outside shell. For the entire domain to be modeled by molecular mechanics, 46,200 atoms were required, which is very expensive computationally. The numerical results were compared with reported experimental values for the failure stress. The model with a certain number of defects agreed much better with the experimental measurements than did a perfect nanotube model.

As aforementioned, carbon nanotube–based electrostatic switches have the potential to operate in the gigahertz range and achieve much higher integration levels than currently possible. As such, modeling attempts to gain insight into the performance of the device pursued. Aluru’s group developed various numerical models, including continuum models, and continuum/MD coupled models to analyze device behavior [92]. This work shows that continuum modeling, considering nonlinear beam theory, is in good agreement with molecular

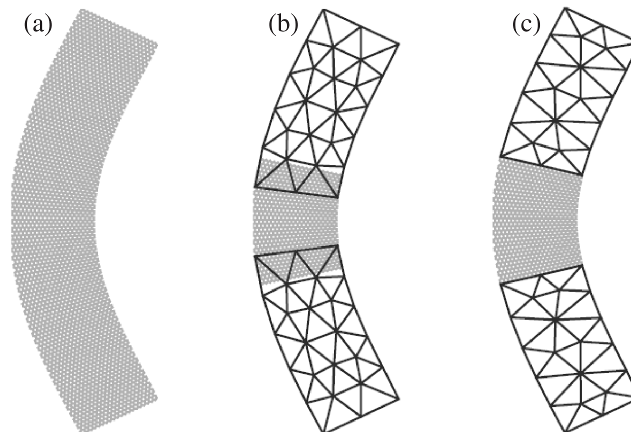

Figure 26. Comparison of bent graphite sheet by means of (a) molecular mechanics, (b) overlapping coupling, (c) edge-to-edge coupling. Reprinted with permission from [91], T. Belytschko et al., *Int. J. Multiscale Comp. Engr.* 1, 115 (2003). © 2003, Begell House, Inc.

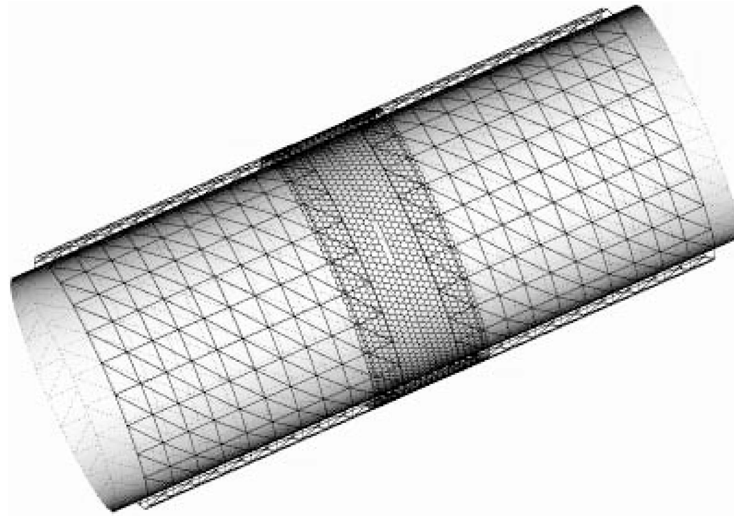

Figure 27. Carbon nanotube model for fracture study by overlapping coupling method. Reprinted with permission from [91], T. Belytschko et al., *Int. J. Multiscale Comp. Engr.* 1, 115 (2003). © 2003, Begell House, Inc.

mechanics modeling. MD simulation showed that, with an increase of the gap between the nanotube and the ground, the nanotube locally buckles as it approaches the ground. The local buckling phenomenon was not captured by the continuum beam theory employed in the analysis. Hence a combined continuum/MD technique was used to overcome this limitation. Figure 28 compares the deformed shapes obtained from the combined continuum/MD model and the fully molecular mechanics model. The buckling that occurred at the two ends of the nanotube was captured by the MD subdomain. In the center of the nanotube, the nonlinear beam theory was able to predict well and greatly reduced the computational cost. The combined continuum/MD approach and the fully MD approach provided good agreement in terms of the static pull-in voltage.

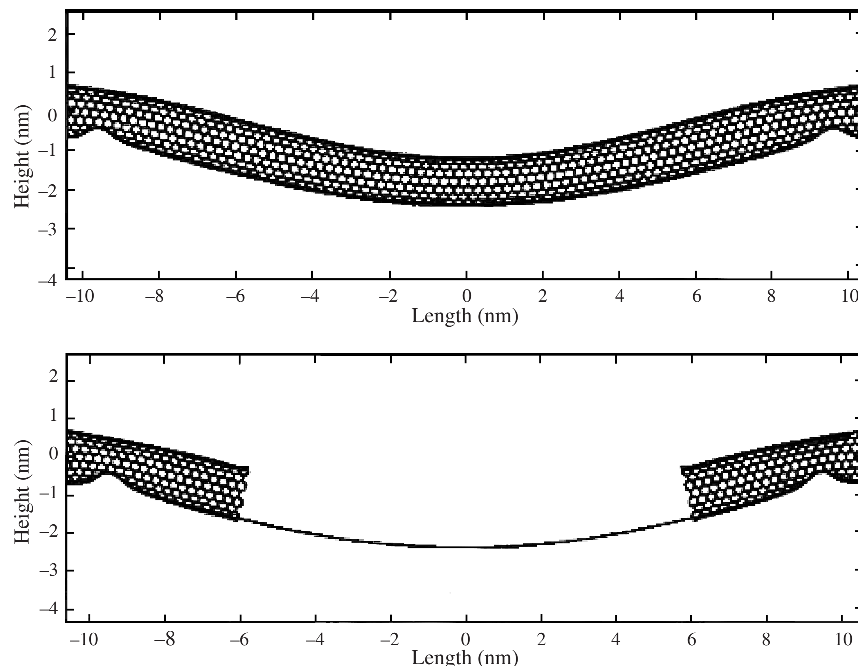

Figure 28. Deformation plot of a fixed-fixed carbon nanotube-based switch. The top figure is the result from full molecular dynamics (MD) simulation and the lower is the multiscale result in which the central region is modeled by one-dimensional nonlinear beam theory. Reprinted with permission from [92], M. Desquenes et al., *J. Eng. Mater. Tech.* 126, 230 (2004). © 2004, American Society of Mechanical Engineers.

Microgears have been one of the most successful MEMS devices so far. Such devices are presently made at the 100 μm scale and rotate at speeds of 150,000 rpm. Next generation of devices (nanogears), based on nanofabrication, are expected to be below the 1 μm level. The effects of wear, lubrication, and friction are expected to have significant consequences on the performance of the nanogears, where areas of contact are an important part of the systems. However, the process of nanogear teeth grinding against each other cannot be simulated accurately with FE because of the bond breaking and formation at the point of contact can only be treated empirically in FE. Alternatively, multiscale modeling provides a good tool to predict the mechanics-related issues for these devices. Figure 29 shows the multiscale decomposition for the modeling of nanogears. An inner region, including the shaft, is discretized by finite elements. The handshaking between the FE and MD region is accomplished by a self-consistent overlap region. In regions at the gear-gear contact point in the nonlubricated case, a tightbinding (TB) description is used as part of a QM simulation [87].

3.2. Continuum Mechanics Modeling

Many NEMS devices can be modeled either as biased cantilever beams or fixed-fixed beams freestanding over a ground substrate, as shown in Fig. 30. The beams can be carbon nanotubes, nanowires, or small nanofabricated parts. The electromechanical characterization of NEMS involves the calculation of the elastic energy (E_{elas}), from the deformation of active components, the electrostatic energy (E_{elec}), and van der Waals energy (E_{vdW}) from atomic interactions. In the following section, we summarize the continuum theory for each of these

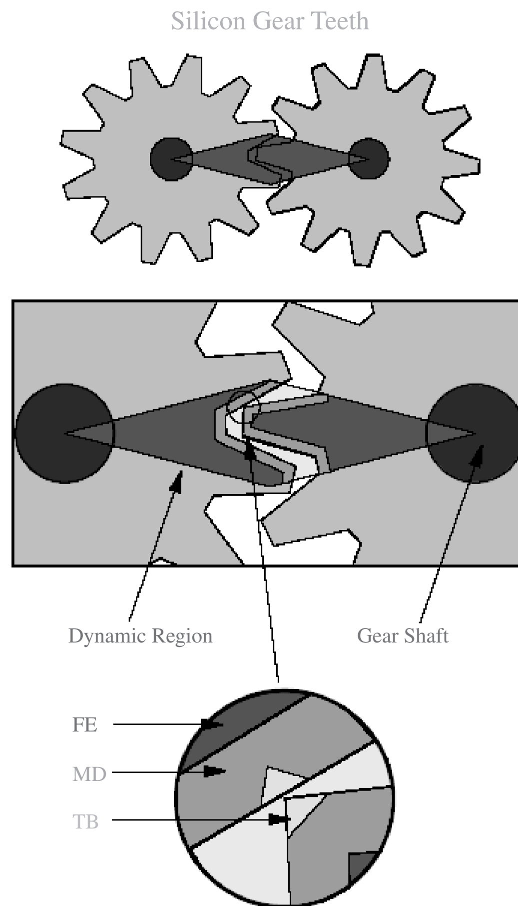

Figure 29. Illustration of dynamic simulation zone and domain decomposition for coupling of length scales: from continuum (FE) to atomistic (MD) to electronic structure (TB). Reprinted with permission from [87], R. E. Rudd and J. Q. Broughton, R. E. Rudd and J. Q. Broughton, *J. Model. Simul. Microsys.* 1, 29 (1999). © 1999, Applied Computational Research Society.

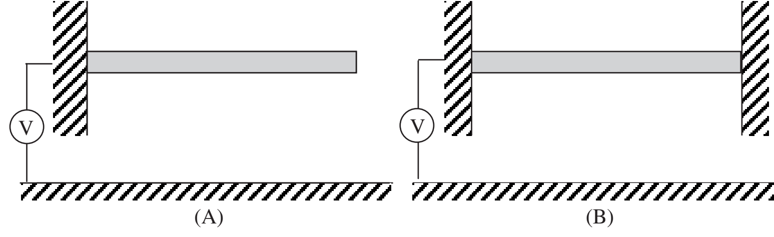

Figure 30. Schematic of NEMS devices. (A) Cantilever beam configuration. (B) Doubly clamped beam configuration.

energy domains and the governing equations of equilibrium for both small deformation and finite deformation. We follow the work reported in Refs. [32, 88, 92, 103, 104, 106].

3.2.1. Continuum Theory

3.2.1.1. Van der Waals Interactions The van der Waals (vdW) energy originates from the interaction between atoms. The Lennard-Jones potential is a suitable model to describe van der Waals interaction [93]. In the Lennard-Jones potential, there are two terms: one is repulsive and the other is attractive. The Lennard-Jones potential between two atoms i and j is given by

$$\phi_{ij} = \frac{C_{12}}{r_{ij}^{12}} - \frac{C_6}{r_{ij}^{6}} \tag{3}$$

where r_{ij} is the distance between atoms i and j and C_6 and C_{12} are attractive and repulsive constants, respectively. For the carbon-carbon interaction, $C_6 = 15.2$ eVÅ^6 and $C_{12} = 24.1$ keVÅ^{12} and the equilibrium spacing $r_0 = 3.414$ Å [94]. From Eq. (3), we can see that the repulsive components of the potential decay extremely fast and play an important role only when the distance is close to or smaller than r_0. The total van der Waals energy can be computed by a pair-wise summation over all the atoms. The computational cost (number of operations) is proportional to the square of the number n of atoms in the system. For a NEMS device with millions of atoms, this technique is prohibitively expensive. Instead, a continuum model was established to compute the van der Waals energy by the double-volume integral of the Lennard-Jones potential [95], that is,

$$E_{\text{vdW}} = \int_{\nu_1}\int_{\nu_2} n_1 n_2 \left(\frac{C_{12}}{r^{12}(\nu_1, \nu_1)} - \frac{C_6}{r^{6}(\nu_1, \nu_1)} \right) d\nu_1 d\nu_1 \tag{4}$$

where, ν_1 and ν_2 represent the two domains of integration, and n_1 and n_1 are the densities of atoms for the domains ν_1 and ν_2, respectively. The distance between any point on ν_1 and ν_2 is $r(\nu_1, \nu_1)$.

Let us consider SWNT freestanding above a ground plane consisting of layers of graphite sheets, with interlayer distance $d = 3.35$ Å, as illustrated in Fig. 31(A). The energy per unit length of the nanotube is given by

$$\frac{E_{\text{vdW}}}{L} = 2\pi\sigma^2 R \sum_{n=1}^{N} \int_{-\pi}^{\pi} \left(\frac{C_{12}}{10[(n-1)d + r_{\text{init}} + R + R\sin\theta]^{10}} - \frac{C_6}{4[(n-1)d + r_{\text{init}} + R + R\sin\theta]^{4}} \right) d\theta \tag{5}$$

where L is the length of the nanotube, R is the radius of the nanotube, r_{init} is the distance between the bottom of the nanotube and the top graphene sheet, N is the number of graphene sheets and $\sigma \cong 38$ nm^{-2} is the graphene surface density. When r_{init} is much larger than the equilibrium spacing r_0, the repulsive component can be ignored and Eq. (5) can be simplified [88] as

$$\frac{E_{\text{vdW}}}{L} = C_6 \sigma^2 \pi^2 R \sum_{r=r_{\text{init}}}^{(N-1)d + r_{\text{init}}} \frac{(R + r)[3R^2 + 2(r + R)^2]}{2[(r + R)^2 - R^2]^{7/2}} \tag{6}$$

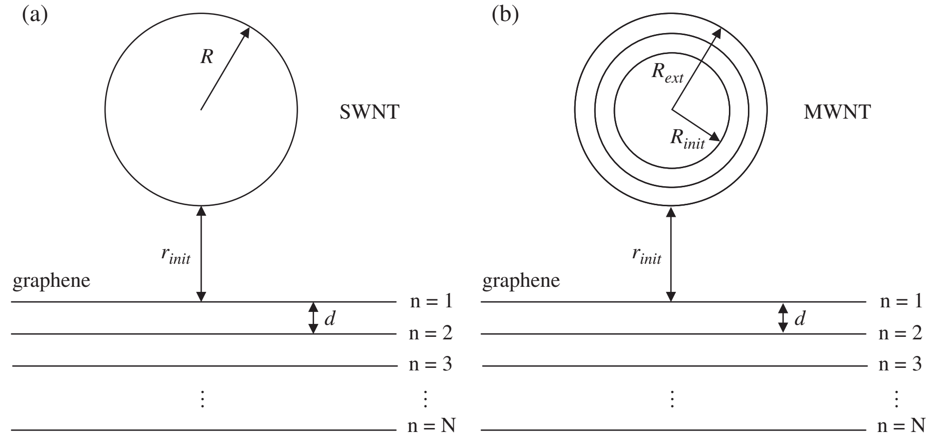

Figure 31. Van der Waals integration of a SWNT (A) and MWNT (B) over a graphite ground plane. Reprinted with permission from [88], M. Desquenes et al., *Nanotechnology* 13, 120 (2002). © 2002, Institute of Physics.

The accuracy of Eq. (6) in approximating the continuum van der Waals energy of a SWNT placed over a graphite plane is verified by the comparison with the direct pair-wise summation of the Lennard-Jones potential given by Eq. (3) for a (16, 0) tube, which is shown in Fig. 32 [88].

For a MWNT, as illustrated in Fig. 31(B), the energy per unit length can be obtained by summing up the interaction between all separate shells and layers:

$$\frac{E_{\mathrm{vdW}}}{L} = \sum_{R=R_{\mathrm{int}}}^{R_{\mathrm{ext}}} \sum_{r=r_{\mathrm{init}}}^{(N-1)d+r_{\mathrm{init}}} \frac{C_6 \sigma^2 \pi^2 R(R+r)[3R^2 + 2(r+R)^2]}{2[(r+R)^2 - R^2]^{7/2}} \tag{7}$$

where R_{int} and R_{ext} are the inner and outer radii of the nanotube, respectively.

The van der Waals force per unit length can be obtained as

$$q_{\mathrm{vdW}} = \frac{d\left(\frac{E_{\mathrm{vdW}}}{L}\right)}{dr} \tag{8}$$

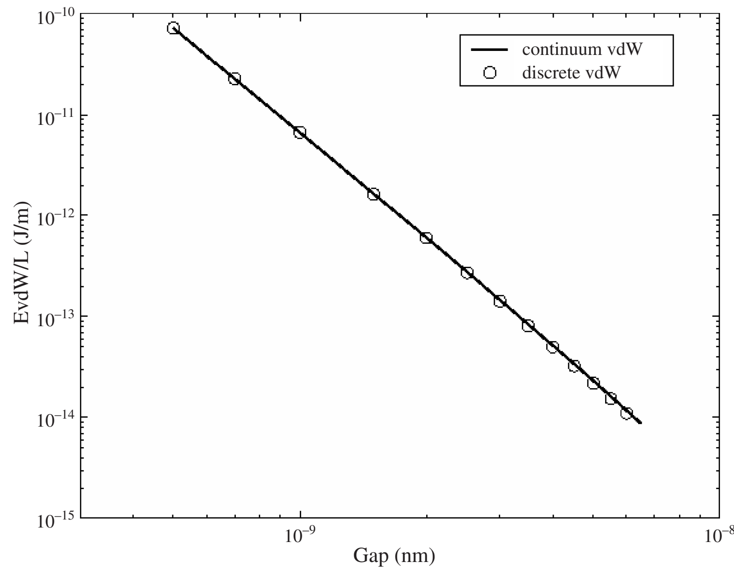

Figure 32. Comparison of the continuum van der Waals (vdW) energy given by Eq. (6) with the discrete pair-wise summation given by Eq. (3). Reprinted with permission from [88], M. Desquenes et al., *Nanotechnology* 13, 120 (2002). © 2002, Institute of Physics.

Thus, inserting Eq. (7) into Eq. (8) and taking the derivative with respect to r, one obtains [88]

$$q_{\mathrm{vdW}} = \sum_{R=R_{\mathrm{int}}}^{R_{\mathrm{ext}}} \sum_{r=r_{\mathrm{init}}}^{(N-1)d+r_{\mathrm{init}}} -\frac{C_6\sigma^2\pi^2 R\sqrt{r(r+2R)}\left(8r^4+32r^3R+72r^2R^2+80rR^3+35R^4\right)}{2\left[2r^5(r+2R)^5\right]^5} \quad (9)$$

3.2.1.2. Electrostatic Force When a biased conductive nanotube is placed above a conductive substrate, there are induced electrostatic charges both on the tube and on the substrate. The electrostatic force acting on the tube can be calculated using a capacitance model [96].

Let us look at the electrostatic force for a conductive nanotube with finite length and round cross section above an infinite ground plane. Although nanotubes have hollow structures, carbon nanotubes with capped ends are more electrochemically stable than those with open ends [97]. Thus, nanotubes with finite length, as well as nanowires, can be geometrically approximated by conductive nanocylinders. For small-scale nanocylinders, the density of states on the surface is finite. The screening length, the distance that the "surface charge" actually penetrates into the cylinder interior, is found to be a nanometer-scale quantity [98]. For nanocylinders with transverse dimension (i.e., diameter approaching the screening length), such as SWNT, the finite size and density of states (quantum effects) have to be considered thoroughly when calculating the surface/volume charge distribution [99, 100]. For nanocylinders with transverse dimension much larger than the screening length, such as MWNT or nanowires with large outer diameter (e.g., 20 nm), this quantum effect can be considered negligible. Thus, the charge distribution can be approximated by the charge distribution on a metallic, perfectly conductive cylinder with the same geometry to which classical electrostatic analysis can be applied.

For infinitely long metallic cylinders, the capacitance per unit length [96] is given by

$$C_d(r) = \frac{\pi\varepsilon}{a\cosh\left(1+\frac{r}{R}\right)} \quad (10)$$

where r is the distance between the lower fiber of the nanocylinder and the substrate, R is the radius of the nanocylinder, and ε is the permittivity of the medium. For vacuum, $\varepsilon_0 = 8.854 \times 10^{-12}\ C^2N^{-1}m^{-2}$. Equation (10) can be applied for infinitely long MWNTs with large diameters ($R = R_{\mathrm{ext}}$).

For the charge distribution on infinite long SWNT, Bulashevich and Rotkin [100], proposed a quantum correction, rendering the capacitance per unit length as

$$C = \frac{C_d}{1+\frac{C_d}{C_Q}} \approx C_d\left(1-\frac{C_d}{C_Q}\right) \quad (11)$$

where $C_Q = e^2 v_m$, and v_M is the constant density of the states near the electroneutral level measured from the Fermi level.

For nanocylinders with finite length, there are two types of boundary surfaces—the cylindrical side surface and the planar end surface. Essentially classical distribution of charge density with a significant charge concentration at the cylinder end has been observed [99, 101, 102]. Here we discuss a model to calculate the electrostatic charge distribution on metallic cylindrical cantilevers based on a boundary element method (BEM), considering both the concentrated charge at the free end and the finite rotation due to the deflection of the cantilever [103].

Figure 33 shows the charge distribution along the length L of a freestanding nanotube, subjected to a bias voltage of 1 V. The contour plot shows the charge density (side view), while the curve shows the charge per unit length along the nanotube. The calculation was performed using the CFD-ACE+ software (a commercial code from CFD Research Corporation based on finite and BEMs). There is significant charge concentration on the free ends and uniform charge distribution in the central of the cantilever, which is found to follow Eq. (10). The charge distribution along a deflected cantilever nanotube is shown in Fig. 34.

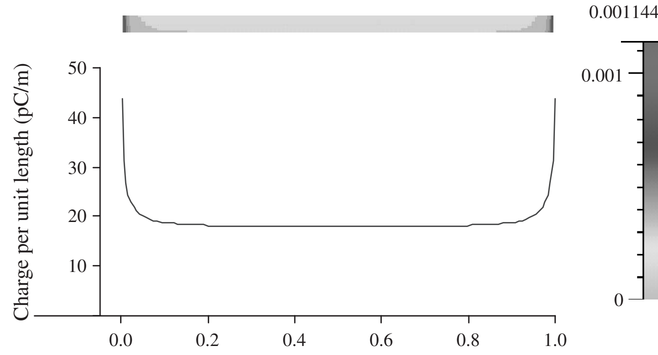

Figure 33. Charge distribution for a biased nanotube. The device parameters are $R_{ext} = 9$ nm, $H = 100$ nm, and $L = 1$ μm. Reprinted with permission from [104], C.-H. Ke et al., *J. Appl. Mech.* in press (2005). © 2005, American Society of Mechanical Engineers.

The parameters are $R_{ext} = 20$ nm, $H = 500$ nm, $L = 3$ μm, and the gap between the free end and the substrate $r(L) = 236$ nm. From Fig. 34, it is seen that, besides the concentrated charge on the free end, the clamped end imposes a significant effect to the charge distribution in the region close to it [98]. However, this effect can be considered negligible because its contribution to the deflection of the nanotube is quite limited. The charge distribution in regions other than the two ends closely follows Eq. (10). A formula for the charge distribution, including end charge effects and the deflection of the cantilever, is derived from a parametric analysis [103], as follows:

$$C(r(x)) = C_d(r(x))\{1 + 0.85[(H+R)^2R]^{1/3}\delta(x - x_{tip})\} = C_d(r(x))\{1 + f_c\} \tag{12}$$

where the first term in the bracket accounts for the uniform charge along the side surface of the tube and the second term, f_c, accounts for the concentrated charge at the end of the tube (for doubly clamped tube, $f_c = 0$). H is the distance between the cantilever and the substrate when the cantilever is in horizontal position, R is the radius of the tube (for MWNT $R = R_{ext}$), $x = x_{tip} = L$ for small deflection (when considering the finite kinematics,

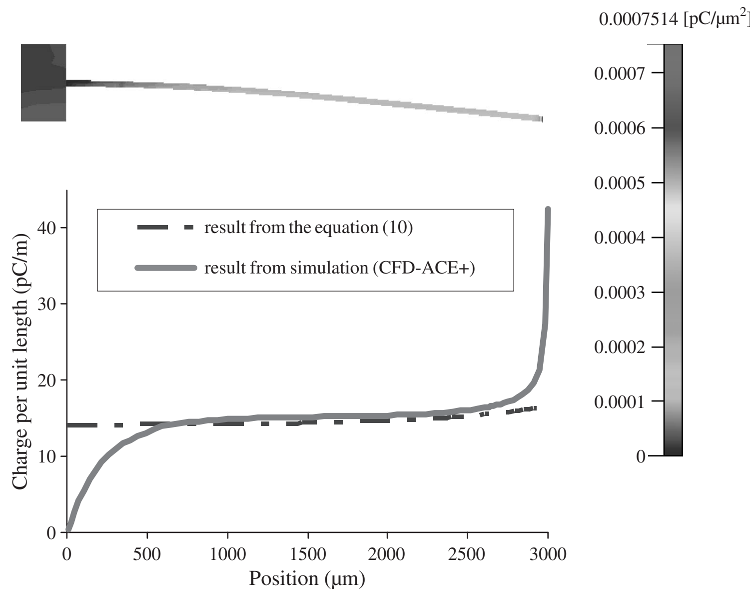

Figure 34. (Top) Two-dimensional side view of the charge distribution in a deflected nanotube cantilever. (Bottom) Charge distribution per unit length along a deflected nanotube cantilever. The solid line is plotted from Eq. (10); the dotted line is the simulation result performed with CFD-ACE+. Reprinted with permission from [103], C.-H. Ke and H. D. Espinosa, *J. Appl. Mech.* in press (2005). © 2005, American Society of Mechanical Engineers.

i.e., large displacement, $x = x_{\text{tip}} \neq L$), $\delta(x)$ is the Dirac function, and $r(x) = H - w(x)$, with w being the tube deflection.

Thus, the electrostatic force per unit length of the nanotube is given by differentiation of the energy [104], as follows:

$$q_{\text{elec}} = \frac{1}{2}V^2\frac{dC}{dr} = \frac{1}{2}V^2\left(\frac{dC_0}{dr}\right)\{1+f_c\} = \frac{-\pi\varepsilon_0 V^2}{\sqrt{r(r+2R)}a\cosh^2\left(1+\frac{r}{R}\right)}(1+f_c) \quad (13)$$

where V is the bias voltage.

3.2.1.3. Elasticity Continuum-beam theory has been widely used to model the mechanics of nanotubes [25, 32, 88, 92, 104–106]. The applicability and accuracy of the continuum theory have been evaluated by comparison with MD simulations [88]. Figure 35 shows the comparison of the deflection of a 20-nm-long, doubly clamped DWNT with a diameter of 1.96 nm, calculated by MD simulation and by the beam equation, respectively. The solid black curve—the deflection predicated by the beam equation—follows closely the shape predicted by MD calculations.

Because nanotubes have high flexibility with strain at tensile failure of the order of 30% [107], nonlinear effects such as finite kinematics, accounting for large displacement need, to be considered in the modeling. This is particularly important for doubly clamped nanotube beams because the stretching from the finite kinematics stiffens the beam, resulting in a significant increase of the pull-in voltage, a key parameter in NEMS devices.

3.2.1.4. Governing Equations The electromechanical characteristic of nanotube cantilevers or doubly clamped nanotube beams can be determined by coupling the van der Waals, electrostatic, and elastic forces. The governing equation under the small deformation assumption (considering only bending) [88] is given by

$$EI\frac{d^4r}{dx^4} = q_{\text{elec}} + q_{\text{vdW}} \quad (14)$$

where r is the gap between the nanotube and the ground plane, x is the position along the tube, E is the Young's modulus (for carbon nanotube $E = 1 - 1.2$ TPa), I is the moment of inertia (for nanotubes, $I = \frac{\pi}{4}(R_{\text{ext}}^4 - R_{\text{int}}^4)$, R_{ext} and R_{int} are the outer and inner radii of the nanotubes, respectively), and q_{elec} and q_{vdW} are given by Eqs. (14) and (9), respectively.

For cantilevers exhibiting large displacements, as shown in Fig. 36, the curvature of the deflection should be considered and the governing equation [104] changes into

$$EI\frac{d^2}{dx^2}\left(\frac{\frac{d^2r}{dx^2}}{\left(1+\left(\frac{dr}{dx}\right)^2\right)^{\frac{3}{2}}}\right) = (q_{\text{vdW}} + q_{\text{elec}})\sqrt{1+\left(\frac{dr}{dx}\right)^2} \quad (15)$$

For doubly clamped structures exhibiting finite kinematics, as shown in Fig. 37, stretching becomes significant as a consequence of the ropelike behavior of a doubly clamped nanotube. The corresponding governing equation [92, 104, 106] is expressed as

$$EI\frac{d^4w}{dx^4} - \frac{EA}{2L}\int_0^L\left(\frac{dw}{dx}\right)^2dx\frac{d^2w}{dx^2} = q_{\text{elec}} + q_{\text{vdW}} \quad (16)$$

where the term $\frac{EA}{2L}\int_0^L(\frac{dw}{dx})^2dx$ is the tension along the axis of the tube due to stretching.

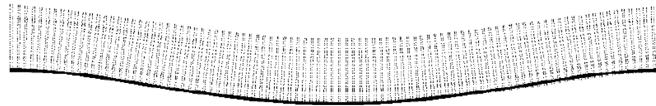

Figure 35. Comparison between MD and beam theory of the deflection of a 20-nm-long fixed-fixed DWNT (diameter 1.96 nm). The solid black curve is the deflection predicated by beam theory. Reprinted with permission from [88], M. Desquenes et al., *Nanotechnology* 13, 120 (2002). © 2002, Institute of Physics.

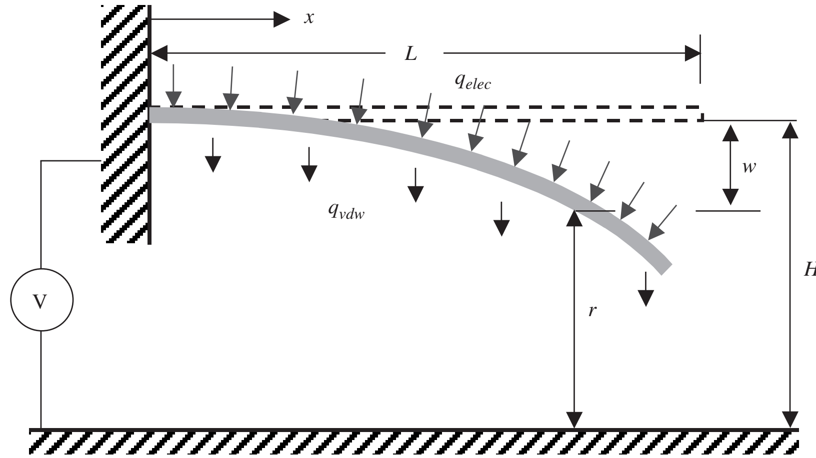

Figure 36. Schematic of finite kinematics configuration of a cantilever nanotube device subjected to electrostatic and van der Waals forces. Reprinted with permission from [104], C.-H. Ke et al., *J. Appl. Mech.* in press (2005). © 2005, American Society of Mechanical Engineers.

The aforementioned governing equations can be numerically solved by either direct integration or finite difference method. The effect of various factors, such as concentrated charge, finite kinematics, and stretching, on the prediction of pull-in voltages of devices can then be identified.

In the following, the effects of concentrated charge and finite kinematics on the prediction of the pull-in voltage for a cantilevered nanotube with $R_{\text{ext}} = 10$ nm, $R_{\text{int}} = 0$, $E = 1$ TPa, $H = 100$ nm, $L = 500$ nm are considered [104]. The displacement of the tip as a function of the applied voltage is shown in Fig. 38. As expected, the role of the finite kinematics becomes negligible. The pull-in voltages, corresponding to the vertical lines, differ by less than 1%. Both numerical solutions reported in Fig. 38 consider the charge concentration at the tip of the cantilevered nanotube. Figure 39 shows the error in the pull-in voltage in case the charge concentration is ignored. It is inferred that the error from neglecting charge concentration can be appreciable.

The effect of finite kinematics and stretching on the prediction of pull-in voltage for a doubly clamped nanotube is examined by investigating a device with the following characteristics $R_{\text{ext}} = 10$ nm, $R_{\text{int}} = 0$, $E = 1$ TPa, $H = 100$ nm, $L = 3000$ nm [104]. The central deflection of the nanotube as a function of the applied voltage is shown in Fig. 40 for both with and without stretching. The two vertical lines correspond to reaching unstable behavior (i.e., pull-in voltages). The role of tension stiffening due to the ropelike behavior is quite pronounced in this case.

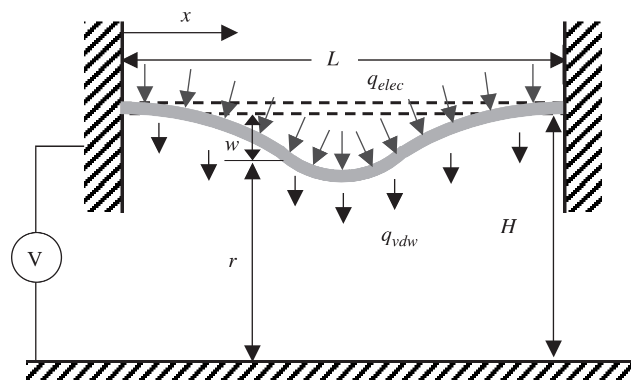

Figure 37. Schematic of finite kinematics configuration of a doubly clamped nanotube device subjected to electrostatic and van der Waals forces. Reprinted with permission from [104], C.-H. Ke et al., *J. Appl. Mech.* in press (2005). © 2005, American Society of Mechanical Engineers.

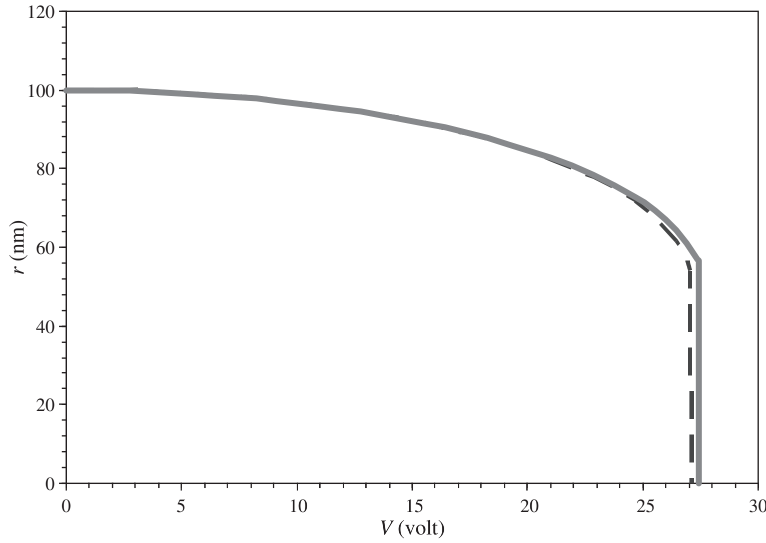

Figure 38. The effect of finite kinematics on the characteristic of the cantilever nanotube based device (tip displacement vs. voltage). The solid lines illustrate the result accounting for finite kinematics, while the dashed line shows the result when finite kinematics is neglected. Both analyses account for charge concentration at the end of the cantilever nanotube. Reprinted with permission from [104], C.-H. Ke et al., *J. Appl. Mech.* in press (2005). © 2005, American Society of Mechanical Engineers.

3.2.2. Analytical Solutions

In this section, we discuss the analytical solutions of the electromechanical characteristic of the NEMS devices consisting of both cantilever and double-clamped nanotubes. In particular, the pull-in voltage calculations based on the energy method are reported [32, 106].

For nanotube cantilevers (singly clamped), the deflection of the cantilever nanotube can be approximated by the following quadratic function [32]:

$$w(s) \approx \frac{x^2}{L^2} c \tag{17}$$

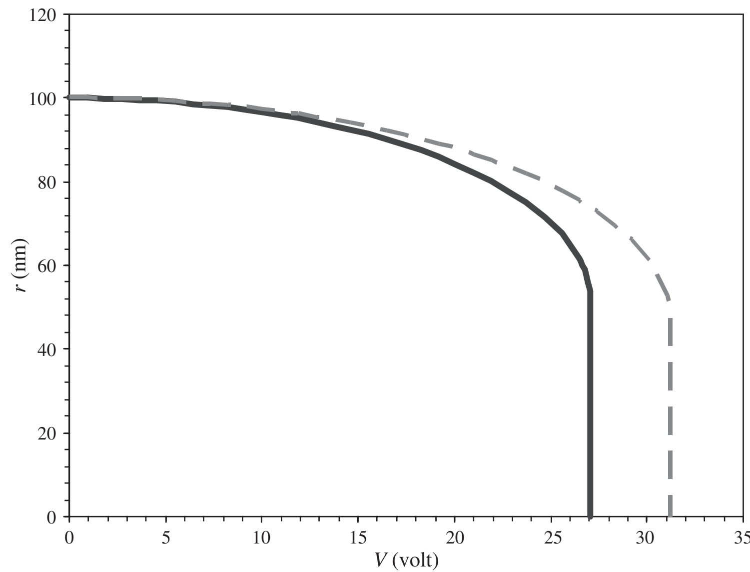

Figure 39. The effect of charge concentration on the characteristic of the cantilever nanotube based device (tip displacement vs. voltage). The solid line illustrates the deflection curve accounting for charge concentration. The dashed line shows the deflection curve in the absence of charge concentration. Both curves are based on the small deflection model. Reprinted with permission from [104], C.-H. Ke et al., *J. Appl. Mech.* in press (2005). © 2005, American Society of Mechanical Engineers.

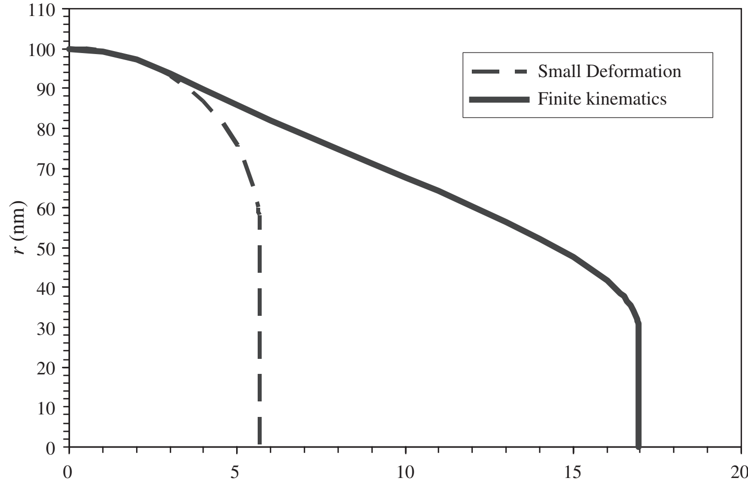

Figure 40. Electromechanical characteristic (central displacement–voltage curve) for doubly clamped nanotube device. The dashed line is for small deformation model (pure bending), and the solid line is for finite kinematics model (bending plus stretching). Reprinted with permission from [106], N. Pugno et al., *J. Appl. Mech.* in press (2005). © 2005, American Society of Mechanical Engineers.

where L is the length of the nanotube, c is a constant that represents the displacement of the end of the cantilever, and x is the coordinate along the nanotube.

The total energy of the system E_{total} is expressed as

$$E_{\text{total}}(c) = E_{\text{elas}}(c) + E_{\text{elec}}(c) + E_{\text{vdW}}(c) \tag{18}$$

where the elastic energy $E_{\text{elas}}(c)$, the electrostatic energy $E_{\text{elec}}(c)$, and van der Waals energy $E_{\text{vdW}}(c)$ can be obtained by integration as

$$E_{\text{elas}}(c) = \frac{EI}{2}\int_0^L \left(\frac{d^2w}{dx^2}\right)^2 dx \tag{19a}$$

$$E_{\text{elec}}(c) \approx \int_0^L \frac{dE_{\text{elec, vdW}}(r(w(x)))}{dx} dx \tag{19b}$$

The equilibrium condition is reached when the total energy reaches a minimum value, that is,

$$\frac{dE_{\text{total}}}{dc} = 0 \tag{20a}$$

Similarly, the instability of the devices (i.e., pull-in) happens when the second-order derivative of total energy equals zero, namely,

$$\frac{d^2E_{\text{total}}}{dc^2} = 0 \tag{20b}$$

The van der Waals interaction plays an important role only for a small gap between the nanotubes and substrate (i.e., a few nanometers). Thus it can be neglected in the analysis of NEMS with large gaps. We consider $E_{\text{vdW}} \approx 0$ in this analysis.

By assuming that the nanotube's (external) radius R_{ext} is much smaller than the distance r between nanotube and ground plane (i.e., $R_{\text{ext}}/r \ll 1$), the pull-in voltage [32], considering the nonlinear finite kinematics and the concentrated charges at the free end, is given by

$$V_{\underset{\text{PI}}{S}} \approx k_S \sqrt{\frac{1+K_S^{\text{FK}}}{1+K_S^{\text{TIP}}}\frac{H}{L^2}\ln\left(\frac{2H}{R_{\text{ext}}}\right)}\sqrt{\frac{EI}{\varepsilon_0}} \tag{21a}$$

$$k_S \approx 0.85, \quad K_S^{\text{FK}} \approx \frac{8H^2}{9L^2}, \quad K_S^{\text{TIP}} \approx \frac{2.55[R_{\text{ext}}(H+R_{\text{ext}})^2]^{1/3}}{L} \tag{21b}$$

where subscripts S refer to singly clamped boundary conditions for cantilevers, superscript FK refers to finite kinematics, and TIP refers to the charge concentration.

For doubly clamped nanotubes, the deflection $w(x)$ is assumed such that it satisfies the boundary conditions $w(x=0,L)=w'(x=0,L)=0$ [106], namely,

$$w(z) \approx 16\left[\left(\frac{x}{L}\right)^2 - 2\left(\frac{x}{L}\right)^3 + \left(\frac{x}{L}\right)^4\right]c \tag{22}$$

where $w(x=L/2)=c$ is here an unknown constant that represents the displacement of the central point. The pull-in voltage [106] can be expressed as

$$V_{\substack{D\\ \mathrm{PI}}} = k_D\sqrt{1+k_D^{\mathrm{FK}}\frac{H+R}{L^2}}\ln\left(\frac{2(H+R)}{R}\right)\sqrt{\frac{EI}{\varepsilon_0}} \tag{23a}$$

$$k_D = \sqrt{\frac{1024}{5\pi S'(c_{\mathrm{PI}})}\left(\frac{c_{\mathrm{PI}}}{H+R}\right)}, \quad k_D^{\mathrm{FK}} = \frac{128}{3003}\left(\frac{c_{\mathrm{PI}}}{\rho}\right)^2 \tag{23b}$$

$$\rho^2 = \frac{I}{A} = \frac{R_{\mathrm{ext}}^2 + R_{\mathrm{int}}^2}{4} \quad S(c) = \sum_{i=1}^{\infty}\left(\frac{1}{\left(\ln\left(\frac{2(H+R)}{R}\right)\right)^i}\sum_{j=i}^{\infty} a_{ij}\left(\frac{c}{(H+R)}\right)^j\right) \tag{23c}$$

Subscripts D refer to double clamped boundary conditions, c_{PI} is the central deflection of the nanotube at the pull-in, and the $\{a_{ij}\}$ in Eq. (23) are known constants [106].

The accuracy of the analytical solutions is verified by the comparison with both numerical integration of the governing equations [104, 106] and experimental measurements (see Section 3.2.3) [32]. The comparison between pull-in voltages evaluated numerically and theoretically for doubly (D) and singly (S) clamped nanotube devices is listed in Table 1 [104]. Columns 6 and 7 in Table 1 compare analytical and numerical pull-in voltage predictions under the assumption of small deformations. Columns 8 and 9 in Table 1 compare analytical and numerical pull-in voltage predictions under the assumption of finite kinematics. The agreement is good (with a maximum discrepancy of 5%).

3.2.3. Comparison Between Analytical Predictions and Experiments

In this section, a comparison between analytical predictions and experimental data, for both small deformation and finite kinematics regimes, is presented.

3.2.3.1. Small Deformation Regime The nanotweezers experimental data reported by Akita et al. 2001 [8], plotted in Fig. 41, is used to assess the model accuracy under small deformation. In this case, the nanotweezers are equivalent to a nanotube cantilever with length of 2.5 μm freestanding above an electrode with a gap of 390 nm. Symmetry is

Table 1. Comparison between pull-in voltages evaluated numerically and theoretically for doubly (D) and singly (S) clamped nanotube devices, respectively; $E = 1$ TPa, $R_{\mathrm{int}} = 0$. For cantilever nanotube device, the symbol (w) denotes that the effect of charge concentration has been included.

Case	BC	H (nm)	L (nm)	$R = R_{\mathrm{ext}}$ (nm)	V_{PI} [V] (theo. linear)	V_{PI} [V] (num. linear)	V_{PI} [V] (theo. nonlinear)	V_{PI} [V] (num. nonlinear)
1	D	100	4000	10	3.20	3.18	9.06	9.54
2	D	100	3000	10	5.69	5.66	16.14	16.95
3	D	100	2000	10	12.81	12.73	36.31	38.14
4	D	150	3000	10	9.45	9.43	38.93	40.92
5	D	200	3000	10	13.53	13.52	73.50	77.09
6	D	100	3000	20	19.21	18.74	31.57	32.16
7	D	100	3000	30	38.57	37.72	51.96	50.63
8	S	100	500	10	27.28 (w)	27.05 (w)	27.52 (w)	27.41 (w)
9	S	100	500	10	27.28 (w)	27.05 (w)	30.87	31.66

Reprinted with permission from [104], C.-H. Ke et al., *J. Appl. Mech.* in press (2005). © 2005, American Society of Mechanical Engineers.

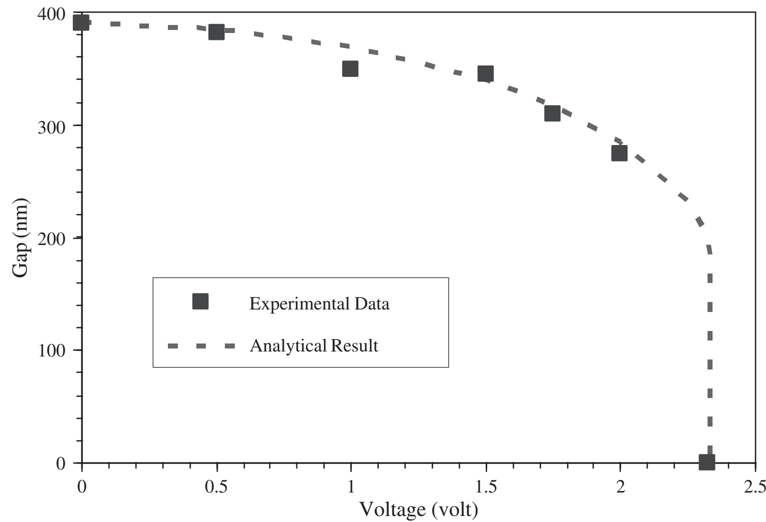

Figure 41. Comparison between experimental data and theoretical prediction in the small deformation regime. Reprinted with permission from [32], C.-H. Ke et al., *J. Mech. Phys. Solids* 53, 1314 (2005). © 2005, Elsevier, Ltd.

exploited. In the same figure, a comparison between the analytically predicted nanotube cantilever deflection and the experimentally measured data are shown [32]. The analytical model includes the van der Waals force and charge concentration at the free end of the nanotube cantilever. Model parameters include Young's modulus, $E = 1$ TPa, external radius $R = R_{ext} = 5.8$ nm, and $R_{int} = 0$. The pull-in voltage from the analytical model is 2.34 V, while the experimentally measured pull-in voltage was 2.33 V. It is clear that the analytical prediction and experimental data for the deflection of the nanotube cantilever, as a function of applied voltage, are in very good agreement.

3.2.3.2. Finite Kinematics Regime Experimental data corresponding to the deflection of carbon nanotube cantilevers in the finite kinematics regime were recently obtained by *in situ* SEM measurements [32].

The configuration of the *in situ* measurement is shown in Fig. 42. The electrode was made of silicon, wafer coated with 50 nm Au film by e-beam evaporation. This Si chip was attached

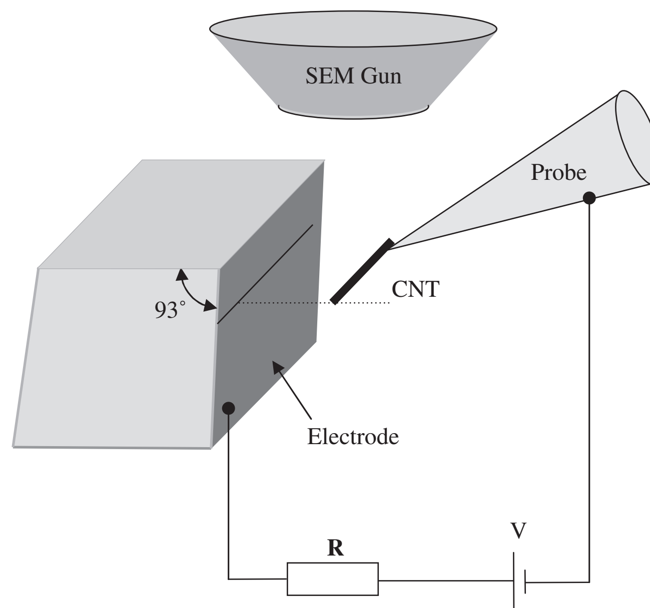

Figure 42. Schematic of the experimental configuration employed in the electrostatic actuation of MWNTs. Reprinted with permission from [32], C.-H. Ke et al., *J. Mech. Phys. Solids* 53, 1314 (2005). © 2005, Elsevier, Ltd.

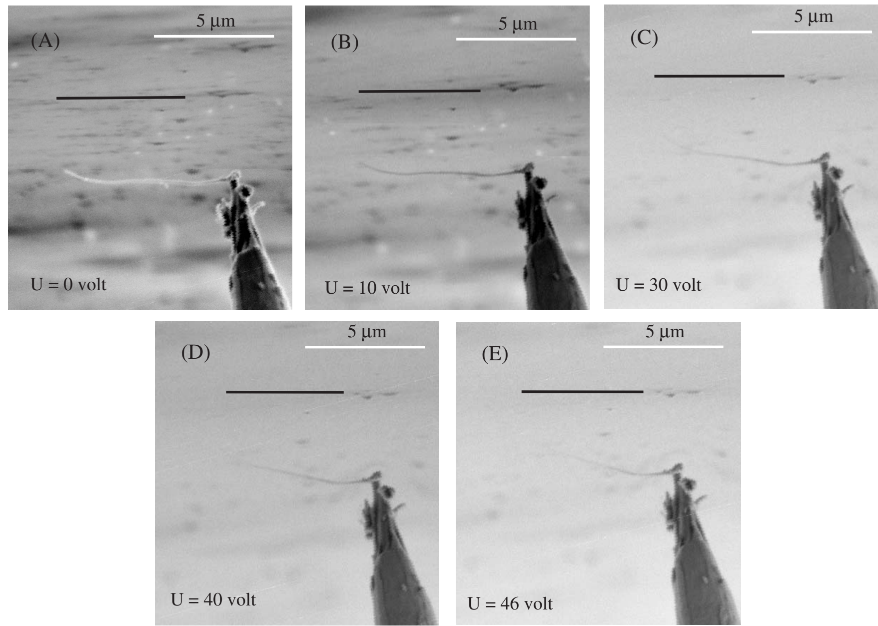

Figure 43. Scanning electron microscopy (SEM) images of the deformed carbon nanotube at various bias voltages. Reprinted with permission from [32], C.-H. Ke et al., *J. Mech. Phys. Solids* 53, 1314 (2005). © 2005, Elsevier, Ltd.

onto the side of a Teflon block and mounted to the SEM sample holder at an angle of 93° with respect to the holder plane. The nanotube cantilever fabricated by the method shown in Fig. 4 was placed horizontally and parallel to the electrode surface as schematically shown in Fig. 42. The distance between the top surface and the electron-beam gun was 5 mm, while the distance between the nanotube and the electron-beam gun was measured to be 6.8 mm. By focusing on the electrode surface and adjusting the working distance to be 6.8 mm, a feature on the electrode, which was on the same horizontal plane with the nanotube, was located. Such a feature is schematically marked as a line in Fig. 42. The horizontal distance between the nanotube and the line was controlled by the nanomanipulator and set to 3 μm. In the circuit, a resistor $R_0 = 1.7$ MΩ was employed to limit the current. Because the ratio between the length of the nanotube and the gap between the nanotube and electrode is 2.3, the deflection of the nanotube can be considered to be in the finite kinematics regime.

Figure 43(A)–43(E) shows the SEM images of the deflection of the carbon nanotube as it is subject to increasing applied voltages. The feature on the electrode, which is in the same

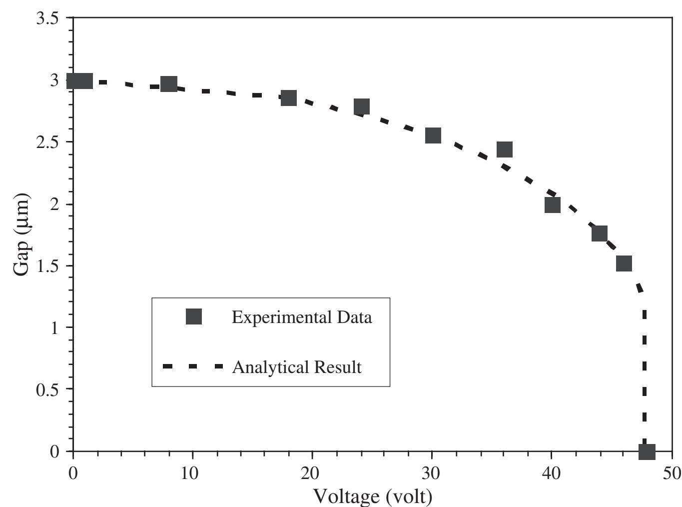

Figure 44. Comparison between experimental data and theoretical prediction in the finite kinematics regime. Reprinted with permission from [32], C.-H. Ke et al., *J. Mech. Phys. Solids* 53, 1314 (2005). © 2005, Elsevier, Ltd.

horizontal plane containing the cantilevered nanotube, is schematically marked as a solid black line in Fig. 43(A)–43(E). These images clearly reveal changes in nanotube deflection and local curvature as a function of applied voltage. A very noticeable effect, although difficult to quantify accurately, is the change in local curvature. The pull-in voltage, V_{PI}, was measured to be 48 V. Through digital image processing, the tip deflection as a function of voltage was measured.

The experimentally measured nanotube cantilever deflections, in the finite kinematics regime, are plotted in Fig. 44 [32]. The figure also shows a comparison between analytical prediction and experimental data. The analytical model includes finite kinematics, the van der Waals force, and charge concentration at the free end of the nanotube cantilever. For these predictions, the following parameters were employed: length of the nanotube, $L = 6.8$ μm; initial gap between nanotube and electrode, $H = 3$ μm; $R = R_{ext} = 23.5$ nm; $R_{int} = 0$, $E = 1$ TPa. The pull-in voltage given by the analytical analysis is 47.8 V, while the pull-in voltage experimentally measured was 48 V.

ACKNOWLEDGMENTS

We would like to express our appreciation to Drs. J. Newcomb and J. Larsen-Base for supporting this work. A special thankyou is due to Y. Zhu, N. Pugno, and N. Moldovan for many useful discussion in relation to nanoscale modeling. We acknowledge the support from the FAA through award no. DTFA03-01-C-00031 and the National Science Foundation (NSF) through award no. CMS-0120866. Work was also supported in part by the Nanoscale Science and Engineering Initiative of the NSF under award no. EEC-0118025.

REFERENCES

1. T. Rueckes, K. Kim, E. Joslevich, G. Y. Tseng, C. Cheung, and C. M. Lieber, *Science* 289, 94 (2000).
2. B. Ilic, H. G. Craighead, and S. Krylov, *J. Appl. Phys.* 95, 3694 (2004).
3. Z. J. Davis, G. Abadal, O. Kuhn, O. Hansen, F. Grey, and A. Boisen, *J. Vac. Sci. Technol. B* 18, 612 (2000).
4. M. L. Roukes, *Physica B* 1, 263 (1999).
5. M. L. Roukes, Technical Digest of the 2000 Solid-State Sensor and Actuator Workshop, 2000.
6. A. N. Cleland and M. L. Roukes, *Appl. Phys. Lett.* 69, 2653 (1996).
7. P. Kim and C. M. Lieber, *Science* 126, 2148 (1999).
8. S. Akita, Y. Nakayama, S. Mizooka, Y. Takano, T. Okawa, Y. Miyatake, S. Yamanaka, M. Tsuji, and T. Nosaka, *Appl. Phys. Lett.* 79, 1691 (2001).
9. A. M. Fennimore, T. D. Yuzvlnsky, W. Q. Han, M. S. Fuhrer, J. Cummings, and A. Zettl, *Nature* 424, 408 (2003).
10. J. Kinaret, T. Nord, and S. Viefers, *Appl. Phys. Lett.* 82, 1287 (2003).
11. C.-H. Ke and H. D. Espinosa, *Appl. Phys. Lett.* 85, 681 (2004).
12. V. Sazonova, Y. Yaish, H. Üstünel, D. Roundy, T. Arias, and P. McEuen, *Nature* 431, 284 (2004).
13. S. Iijima, *Nature* 354, 56 (1991).
14. P. Ajayan, *Chem. Rev.* 99, 1787 (1999).
15. C. Journet, W. K. Maser, P. Bernier, A. Loiseau, M. L. delaChapelle, S. Lefrant, P. Deniard, R. Lee, and J. E. Fischer, *Nature* 388, 756 (1997).
16. T. W. Ebbesen and P. M. Ajayan, *Nature* 358, 220 (1992).
17. A. Thess, R. Lee, P. Nikolaev, H. J. Dai, P. Petit, J. Robert, C. H. Xu, Y. H. Lee, S. G. Kim, A. G. Rinzler, D. T. Colbert, G. E. Scuseria, D. Tomanek, J. E. Fischer, and R. E. Smalley, *Science* 273, 483 (1996).
18. W. Z. Li, S. S. Xie, L. X. Qian, B. H. Chang, B. S. Zou, W. Y. Zhou, R. A. Zhao, and G. Wang, *Science* 274, 1701 (1996).
19. D. Qian, G. J. Wagner, W. K. Liu, M. F. Yu, and R. S. Ruoff, *Appl. Mech. Rev.* 55, 495 (2002).
20. P. L. McEuen, M. S. Fuhrer, and H. Park, *IEEE Trans. Nanotechnol.* 1, 78 (2002).
21. T. W. Tombler, C. W. Zhou, L. Alexseyev, J. Kong, H. J. Dai, L. Lei, C. S. Jayanthi, M. J. Tang, and S. Y. Wu, *Nature* 405, 769 (2000).
22. B. Liu, H. T. Johnson, and Y. Huang, *J. Mech. Phys. Solids* 52, 1 (2004).
23. T. Kuzumaki and Y. Mitsuda, *Appl. Phys. Lett.* 85, 1250 (2004).
24. A. Husain, J. Hone, H. W. Ch. Postma, X. M. H. Huang, T. Drake, M. Barbic, A. Scherer, and M. L. Roukes, *Appl. Phys. Lett.* 83, 1240 (2003).
25. E. W. Wong, P. E. Sheehan, and C. M. Lieber, *Science* 277, 1971 (1997).
26. P. A. Williams, S. J. Papadakis, A. M. Patel, M. R. Falvo, S. Washburn, and R. Superfine, *Appl. Phys. Lett.* 82, 805 (2003).
27. R. M. I. Taylor and S. R., in "Advanced Interfaces to Scanning Probe Microscopes" (H. S. Nalwa, Ed.), Vol. 2. Academic, New York, 1999.

28. M. R. Falvo, G. J. Clary, R. M. Taylor, V. P. Chi, F. P. Brooks, S. Washburn, and R. Superfine, *Nature* 389, 582 (1997).
29. M. R. Falvo, R. M. Taylor, A. Helser, V. P. Chi, F. P. Brooks, S. Washburn, and R. Superfine, *Nature* 397, 236 (1999).
30. M. F. Yu, M. J. Dyer, G. D. Skidmore, H. W. Rohrs, X. K. Lu, K. D. Ausman, J. R. von Her, and R. S. Ruoff, *Nanotechnology* 10, 244 (1999).
31. M. F. Yu, O. Lourie, M. J. Dyer, K. Moloni, T. F. Kelly, and R. S. Ruoff, *Science* 287, 637 (2000).
32. C.-H. Ke, N. Pugno, B. Peng, and H. D. Espinosa, *J. Mech. Phys. Solids* 53, 1314 (2005).
33. P. A. Smith, C. D. Nordquist, T. N. Jackson, T. S. Mayer, B. R. Martin, J. Mbindyo, and T. E. Mallouk, *Appl. Phys. Lett.* 77, 1399 (2000).
34. X. Q. Chen, T. Saito, H. Yamada, and K. Matsushige, *Appl. Phys. Lett.* 78, 3714 (2001).
35. J. Chung and J. Lee, *Sens. Actuators A* 104, 229 (2003).
36. M. P. Hughes and H. Morgan, *J. Phys. D* 31, 2205 (1998).
37. M. P. Hughes, in "Handbook of Nanoscience, Engineering and Technology" (B. D., S. Lyshevski, G. Iafrate, and W. A. Goddard III, Eds.). CRC Press, 2002.
38. A. Ramos, H. Morgan, N. G. Green, and A. Castellanos, *J. Phys. D* 31, 2338 (1998).
39. K. Yamamoto, S. Akita, and Y. Nakayama, *J. Phys. D* 31, L34 (1998).
40. R. Krupke, F. Hennrich, H. Löhneysen, and M. M. Kappes, *Science* 301, 344 (2003).
41. S. Lee, D. Lee, R. Morjan, S. Jhang, M. Sveningsson, O. Nerushev, Y. Park, and E. Campbell, *Nano Lett.* 4, 2027 (2004).
42. Y. Huang, X. F. Duan, Q. Q. Wei, and C. M. Lieber, *Science* 291, 630 (2001).
43. M. Fujiwara, E. Oki, M. Hamada, Y. Tanimoto, I. Mukouda, and Y. Shimomura, *J. Phys. Chem. A* 105, 4383 (2001).
44. S. M. Huang, L. M. Dai, and A. W. H. Mau, *J. Phys. Chem. B* 103, 4223 (1999).
45. J. Kong, H. T. Soh, A. M. Cassell, C. F. Quate, and H. Dai, *Nature* 395, 878 (1998).
46. H. J. Dai, *Physics World* 13, 43 (2000).
47. Y. Zhang, A. Chang, J. Cao, Q. Wang, W. Kim, Y. Li, N. Morris, E. Yenilmez, J. Kong, and H. Dai, *Appl. Phys. Lett.* 79, 3155 (2001).
48. H. J. Dai, *Acc. Chem. Res.* 35, 1035 (2002).
49. S. Rao, L. Huang, W. Setyawan, and S. Hong, *Nature* 425, 36 (2003).
50. R. D. Piner, J. Zhu, F. Xu, S. Hong, and C. A. Mirkin, *Science* 283, 661 (1999).
51. M. L. Roukes, *Physics World* 14(2) (2001).
52. R. L. Badzey, G. Zolfagharkhani, A. Gaidarzhy, and P. Mohanty, *Appl. Phys. Lett.* 85, 3587 (2004).
53. H. G. Craighead, *Science* 290, 1532 (2000).
54. Y. Zhu, N. Moldovan, and H. D. Espinosa, *Appl. Phys. Lett.* 86, 013506 (2005).
55. M. Zalalutdinov, B. Ilic, D. Czaplewski, A. Zehnder, H. G. Craighead, and J. M. Parpia, *Appl. Phys. Lett.* 77, 3287 (2000).
56. M. J. Treacy, T. W. Ebbesen, and J. M. Gibson, *Nature* 381, 678 (1996).
57. P. Poncharal, Z. L. Wang, D. Ugarte, and W. A. de Heer, *Science* 283, 1513 (1999).
58. D. S. Greywall, B. Yurje, P. A. Busch, A. N. Pargellis, and R. L. Willett, *Phys. Rev. Lett.* 72, 2992 (1994).
59. A. N. Cleland and M. L. Roukes, *Sens. Actuators A* 72, 256 (1999).
60. K. L. Ekinci, Y. T. Yang, X. M. H. Huang, and M. L. Roukes, *Appl. Phys. Lett.* 81, 2253 (2002).
61. P. Mohanty, D. A. Harrington, K. L. Ekinci, Y. T. Tang, M. J. Murphy, and M. L. Roukes, *Phys. Rev. B* 66, 085416 (2002).
62. M. S. Dresselhaus, G. Dresselhaus, and P. Avouris, "Carbon Nanotubes." Springer, Berlin, 2001.
63. H. Dai, J. H. Hafner, A. G. Rinzler, D. T. Colbert, and R. E. Smalley, *Nature* 384, 147 (1996).
64. S. S. Wong, E. Joselevich, A. T. Woolley, C. L. Cheung, and C. M. Lieber, *Nature* 394, 52 (1998).
65. L. M. Jonsson, S. Axelsson, T. Nord, S. Viefers, and J. M. Kinaret, *Nanotechnology* 15, 1497 (2004).
66. S. J. Tan, A. R. Verschueren, and C. Dekker, *Nature* 393, 49 (1998).
67. C. W. Zhou, J. Kong, and H. J. Dai, *Phys. Rev. Lett.* 84, 5604 (2000).
68. E. D. Minot, Y. Yaish, V. Sazonova, and P. L. McEuen, *Nature* 428, 536 (2004).
69. J. Hu, O. Min, P. Yang, and C. M. Lieber, *Nature* 399, 48 (1999).
70. J. Hu, T. W. Odom, and C. M. Lieber, *Acc. Chem. Res.* 32, 435 (1999).
71. A. M. Morales and C. M. Lieber, *Science* 279, 208 (1998).
72. D. P. Yu, C. S. Lee, I. Bello, X. S. Sun, Y. H. Tang, G. W. Zhou, Z. G. Bai, Z. Zhang, and S. Q. Feng, *Solid State Commun.* 105, 403 (1998).
73. C. Ji and P. C. Searson, *Appl. Phys. Lett.* 81, 4437 (2002).
74. T. C. Wong, C. P. Li, R. Q. Zhang, and S. T. Lee, *Appl. Phys. Lett.* 84, 407 (2004).
75. S. Bhattacharyya, S. K. Saha, and D. Chakravorty, *Appl. Phys. Lett.* 77, 3770 (2000).
76. M. Barbic, J. J. Mock, D. R. Smith, and S. Schultz, *J. Appl. Phys.* 91, 9341 (2002).
77. G. Malandrino, S. T. Finocchiaro, and I. L. Fragalà, *J. Mater. Chem.* 14, 2726 (2004).
78. J. R. Heath and F. K. Legoues, *Chem. Phys. Lett.* 208, 263 (1993).
79. A. B. Greytak, L. J. Lauhon, M. S. Gudiksen, and C. M. Lieber, *Appl. Phys. Lett.* 84, 4176 (2004).
80. K. J. Ziegler, D. M. Lyons, J. D. Holmes, D. Erts, B. Polyakov, H. Olin, K. Svensson, and E. Olsson, *Appl. Phys. Lett.* 84, 4074 (2004).
81. Y. Wu and P. Yang, *Chem. Mater.* 12, 605 (2000).

82. D. Banerjee, J. Y. Lao, D. Z. Wang, J. Y. Huang, Z. F. Ren, D. Steeves, B. Kimball, and M. Sennett., *Appl. Phys. Lett.* 83, 2061 (2003).
83. Y. Dai, Y. Zhang, Y. Q. Bai, and Z. L. Wang, *Chem. Phys. Lett.* 375, 96 (2003).
84. J. J. Mock, S. J. Oldenburg, D. R. Smith, D. A. Schultz, and S. Schultz, *Nano Lett.* 2, 465 (2002).
85. K.-H. Kim, N. Moldovan, and H. D. Espinosa, *Small* 1, 632 (2005).
86. M. D. LaHye, O. Buu, B. Camarota, and K. C. Schwab, *Science* 304, 74 (2004).
87. R. E. Rudd and J. Q. Broughton, *J. Model. Simul. Microsys.* 1, 29 (1999).
88. M. Desquenes, S. V. Rotkin, and N. R. Alaru, *Nanotechnology* 13, 120 (2002).
89. J. A. Moriarty, J. F. Belak, R. E. Rudd, P. Soderlind, F. H. Streitz, and L. H. Yang, *J. Phys.* 14, 2825 (2002).
90. T. Belytschko, W. K. Liu, and B. Moran, "Nonlinear Finite Elements for Continua and Structures." Wiley, 2000.
91. T. Belytschko and S. P. Xiao, *Int. J. Multiscale Comp. Engr.* 1, 115 (2003).
92. M. Desquenes, Z. Tang, and N. R. Aluru, *J. Eng. Mater. Tech.* 126, 230 (2004).
93. J. E. Lennard-Jones, *Proc. R. Soc. A* 129, 598 (1930).
94. L. A. Girifalco, M. Hodak, and R. S. Lee, *Phys. Rev. B* 62, 13104 (2000).
95. L. A. Girifalco, *J. Phys. Chem.* 96, 858 (1992).
96. W. Hayt and J. Buck, "Engineering Electromagnetics," 6th Edn. McGraw-Hill, New York, 2001.
97. L. Lou, P. Nordlander, and R. E. Smalley, *Phys. Rev. B* 52, 1429 (1995).
98. M. Krčmar, W. M. Saslow, and A. Zangwill, *J. Appl. Phys.* 93, 3495 (2003).
99. S. V. Rotkin, V. Shrivastava, K. A. Bulashevich, and N. R. Aluru, *Int. J. Nanosci.* 1, 337 (2002).
100. K. A. Bulashevich and S. V. Rotkin, *JETP Lett.* 75, 205 (2002).
101. W. R. Smythe, *J. Appl. Phys.* 27, 917 (1956).
102. P. Keblkinski, S. K. Nayak, P. Zapol, and P. M. Ajayan, *Phys. Rev. Lett.* 89, 255503 (2002).
103. C.-H. Ke and H. D. Espinosa, *J. Appl. Mech.* in press (2005).
104. C.-H. Ke, H. D. Espinosa, and N. Pugno, *J. Appl. Mech.* in press (2005).
105. J. P. Salvetat, A. J. Kulik, J. M. Bonard, G. A. D. Briggs, T. Stockli, K. Metenier, S. Bonnamy, F. Beguin, N. A. Burnham, and L. Forro, *Adv. Mater.* 11, 161 (1999).
106. N. Pugno, C.-H. Ke, and H. D. Espinosa, *J. Appl. Mech.* in press (2005).
107. B. I. Yakobson, M. P. Campbell, C. J. Brabec, and J. Bernholc, *Comp. Mater. Sci.* 8, 341 (1997).